




## Article

# The Multiple Stages of Regional Triassic Crustal Reworking in Eastern Tianshan, NW China: Evidence from the Xigebi Area

Ming Wei <sup>1</sup>, Haiquan Li <sup>2,3</sup> , Wenxiao Zhou <sup>2,\*</sup> , Mahemuti Muredili <sup>4</sup>, Ernest Chi Fru <sup>5</sup>  and Thomas Sheldrick <sup>6</sup>

<sup>1</sup> The Second Geological Brigade of Xizang Autonomous Region Geological and Mineral Exploration and Development Bureau, Lhasa 850000, China; 13980459480@139.com

<sup>2</sup> Institute of Natural Resources Survey, China University of Geosciences, Wuhan 430074, China; lhq@cug.edu.cn

<sup>3</sup> Xi'an Center of Mineral Resources Survey, China Geological Survey, Xi'an 710100, China

<sup>4</sup> PetroChina Xinjiang Oilfield Company, Karamay 834000, China; 18999758892@163.com

<sup>5</sup> School of Earth and Environmental Sciences, Centre for Geobiology and Geochemistry, Cardiff University, Cardiff CF10 3AT, UK; chifru@cardiff.ac.uk

<sup>6</sup> Department of Geology, University of Leicester, Leicester LE1 7RH, UK; thomassheldrick@gmail.com

\* Correspondence: zhouwenxiao@cug.edu.cn

## Abstract

The eastern Tianshan region in the Central Asian Orogenic Belt (CAOB) is characterized by multiple complex tectonic activity of uncertain historical contribution to the construction of the CAOB. This study utilizes a multi-proxy geochemical approach to characterize I-type monzogranite pluton rocks and their associated hornblende-rich dioritic enclaves to decipher the tectonic and magmatic evolution of the Xigebi area, eastern Tianshan. Zircon geochronology indicates a Triassic and Permian crystallization age of ca.  $224.2 \pm 1.7$  Ma and ca.  $268.3 \pm 3.0$  Ma for the host monzogranites and the dioritic enclaves, respectively. Major, trace and rare earth element distribution, together with Hf isotope systematics displaying noticeable positive  $\epsilon_{\text{Hf}}(t)$  anomalies for both rock types, point to partial melting of meta-mafic rocks in an intraplate extensional setting. The diorite was formed by the melting of lower crustal meta-igneous rocks mixed with mantle melts, and the monzogranite, predominantly from deep crustal meta-basalts contaminated by shallow metasedimentary rocks, with some degree of mixing with deeply sourced mantle magma. While both the host monzogranites and their dioritic enclaves are the products of upwelling magma, the younger Triassic monzogranites captured and preserved fragments of the dioritic Permian lower continental crust during crystallization. These multiple stages of magmatic underplating and crustal reworking associated with vertical stratification of the juvenile paleo-continental crust suggest the monzogranites and diorites indicate a change from a post-collisional setting to a regional intraplate regime on the southern margin of the CAOB.

**Keywords:** granite; Hbl-rich dioritic enclave; geochemistry; zircon U-Pb age; eastern Tianshan; Central Asian Orogenic Belt



Academic Editor: Dmitry Konopelko

Received: 28 June 2025

Revised: 28 July 2025

Accepted: 30 July 2025

Published: 4 August 2025

**Citation:** Wei, M.; Li, H.; Zhou, W.; Muredili, M.; Fru, E.C.; Sheldrick, T. The Multiple Stages of Regional Triassic Crustal Reworking in Eastern Tianshan, NW China: Evidence from the Xigebi Area. *Minerals* **2025**, *15*, 829. <https://doi.org/10.3390/min15080829>

**Copyright:** © 2025 by the authors. Licensee MDPI, Basel, Switzerland. This article is an open access article distributed under the terms and conditions of the Creative Commons Attribution (CC BY) license (<https://creativecommons.org/licenses/by/4.0/>).

## 1. Introduction

The Central Asian Orogenic Belt (CAOB, Figure 1a) is a complex orogenic system composed of multiple oceanic island arcs and microcontinental blocks. As one of the largest Phanerozoic accretionary orogens it records a critical component of Earth's geologic history, which includes the evolution of northern China [1]. The CAOB formed following the break-up of the Rodinia supercontinent, with the subduction of the Paleo-Asian Ocean

(PAO) and the accretion of continental blocks initiated by plate collision [1–8]. Being one of the most actively researched orogenic belts in the world, with most studies focused on Paleozoic magmatism [9–20], a unified consensus on interpretation of geological records, tectonism, and metallogeny with respect to evolution of the CAOBS remains to be achieved. The recent recognition of a high prevalence of Mesozoic rocks than previously thought in Central Asia provides a new opportunity for deepening our understanding of the tectonic and geologic history of the CAOBS [16,21–29].

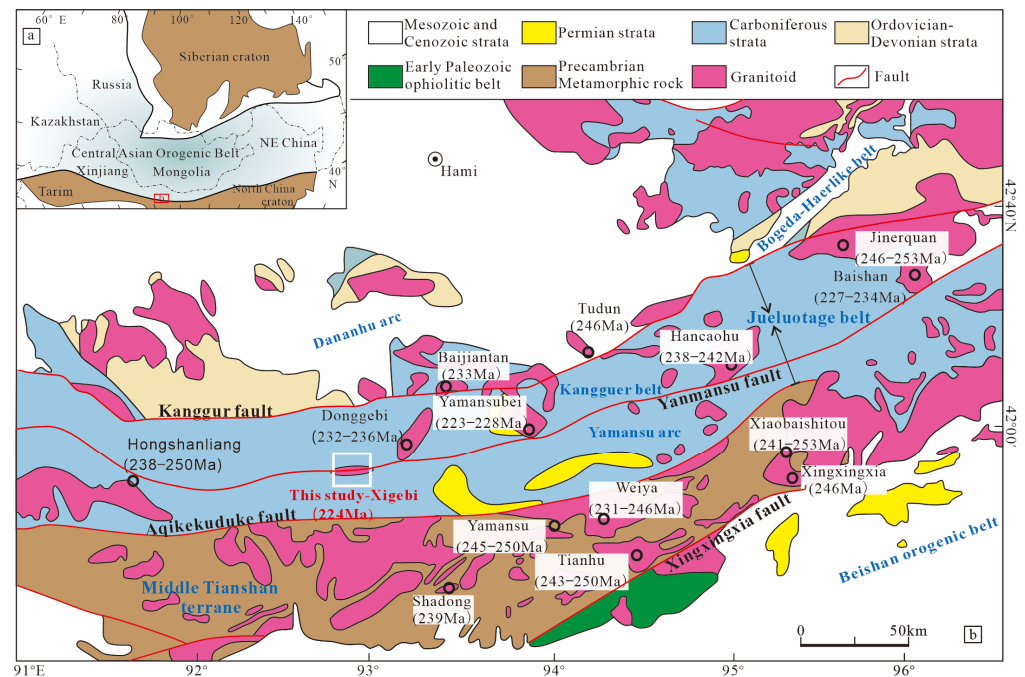


**Figure 1.** (a) Tectonic framework of the Central Asian Orogenic Belt and its adjacent tectonic units. (b) Geological map of eastern Tianshan (modified after Li, Yang [30]).

Particularly, the Tianshan orogenic belt, located southwest of the CAOBS (Figure 1b), between the Junggar Terrane and the Tarim Craton, is associated with numerous branched paleo-oceanic basins developed during its evolution. Since the Neoproterozoic, multiple stages of magmatism and tectonism affected the growth of the eastern Tianshan orogenic belt, which is thought to be related to the movement of massive microcontinental and oceanic blocks [24–27,30–37]. This included the subduction and closing of the northern Tianshan Ocean from the Neoproterozoic, the southern Tianshan Ocean from the Silurian, and subduction of other small oceans, when different microcontinental blocks collided. Since the Permian, a post-collisional regime prevailed in the eastern Tianshan region [19,21,25–27,30,32–35,38–40], leading to a growth in momentum in deciphering the associated tectonic and magmatic processes. In part, this interest has arisen because of recent studies on Mesozoic granitic porphyry Mo deposits highlighting the potential of this region for significant ore deposit formation [25–27,35].

Although most of eastern Tianshan is covered by sediments, there are many Mesozoic magmatic outcrops and contemporaneous metallogenetic deposits found in the Xigebei area, near the Yamansu Fault Belt (Figure 1b). Thus, this study focusses on a Mesozoic pluton that contains dark hornblende (Hbl)-rich dioritic enclaves from the Xigebei area. We compare the newly acquired data with those from magmatic rocks from the Jueluotage Belt and the Weiya granites from the middle Tianshan terrane because they also contain massive dark enclaves [21]. Such enclaves provide an excellent opportunity to study the magmatic and tectonic evolution of the area.

## 2. Geological Setting and Petrography

### 2.1. Geological Setting

The Xigebi area is located on the Yamansu Arc in the southern part of the Jueluotage Belt (Figure 1), where the Wutongwozi formation, Dikaner formation, Aqishnan Group, and the Yamansu Group clastic sedimentary sequences are widespread. The tectonic structure of the Jueluotage Belt was controlled by the Kanggur and Aqikekuduke faults, with the Yamansu fault further subdividing the Jueluotage Belt into the Yamansu Arc and the Kanggur Belt. Ophiolitic mélanges are sparsely distributed in the Kanggur Belt [31], and since the Paleozoic, episodic magmatism has generated igneous rocks of mainly intermediate-felsic composition.

Paleozoic intrusions in the Jueluotage Orogenic Belt, particularly the Carboniferous magmatic rocks, record subduction-related geochemical signatures [16]. While Permian intrusions appear as basic-ultrabasic complexes [12,15] and as contemporaneous A-type and I-type granites [41,42] which are frequently covered by later Permian sediments. Triassic felsic rocks also intrude the Baishan [26,27], Donggebi [25], Xigebi, Yamansu [24], Hongshanliang [40], and the Weiya intrusive complex [21] in the eastern Tianshan area (Figure 1).

This study focuses on an area adjacent to the central Yamansu Fault (Figure 2), where geological surveys have revealed multiple periods of magmatic activity since the Carboniferous Period. Paleozoic-Mesozoic intrusive rocks discovered east of the Xigebi area collectively belong to the same intrusive complex. Mineralogical composition indicates that most of the rock types are either of a dioritic or granitic affinity. Further, Middle Permian low silica hornblende-rich diorites, encapsulated as dark enclaves in the late Triassic plutonic monzogranites, provide new insights into material and energy exchange between the crust and the mantle, and in unravelling the genesis of granite.

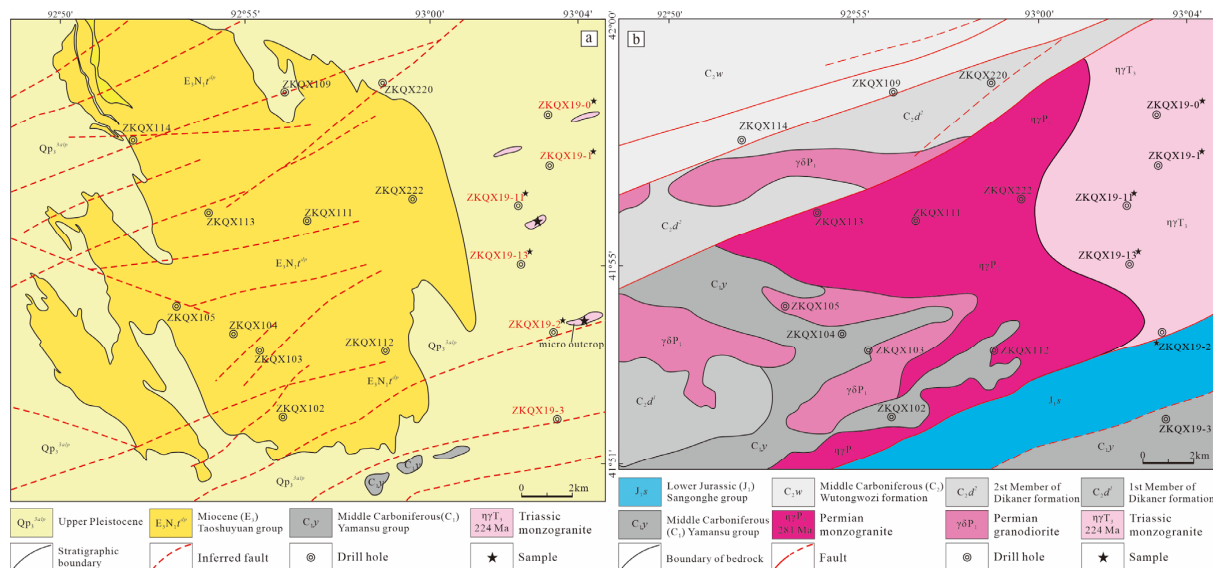


**Figure 2.** (a) Surface geological map of Xigebi showing the sample area. (b) The bedrock map was drawn based on data obtained via drilling endeavors and regional gravity and magnetic data.

### 2.2. Petrography

The contact between the diorite and monzogranite ranges from sharp to gradational, with the lithologies having distinct textures (Figure 3). The fresh fine-grained Hbl-rich dioritic enclaves range in size from 1 cm to 10 m, are commonly rounded, and appear as distinct small dark angular grey-black masses crossed by late veinlets and joints (Figure 3a,b,d,e). Rock samples exhibit subhedral granular minerals, with a porphyritic texture and massive structure. Approximately 5% of the phenocrysts contain plagioclase (Figure 3b), with some



grains displaying potassic alteration (Figure 3d). The plagioclase crystals are subhedral to xenomorphic, with grain sizes of 2–10 mm. The matrix comprises ~95% of the rock, containing ~65% plagioclase, ~30% hornblende, ~2% quartz, and ~3% accessory minerals (Figure 3d,e). The plagioclase crystals range in size from 0.2 to 1.5 mm, are euhedral to subhedral, and exhibit plate-prismatic shapes, with obvious crystal twinning and zonation. Several other minerals are also visible in thin section, including sericite and kaolinite. Hornblende crystal lengths range from 0.2 to 2.0 mm in size. Most of the crystals are long, columnar, and altered, with the alteration resulting in embayment along crystal edges, displaying colors that change from green to brownish yellow. Quartz crystals are less than 0.3 mm and form granular xenomorphs with undulatory extinction. Accessory minerals include magnetite, apatite, and ilmenite, all being less than 0.3 mm in size.

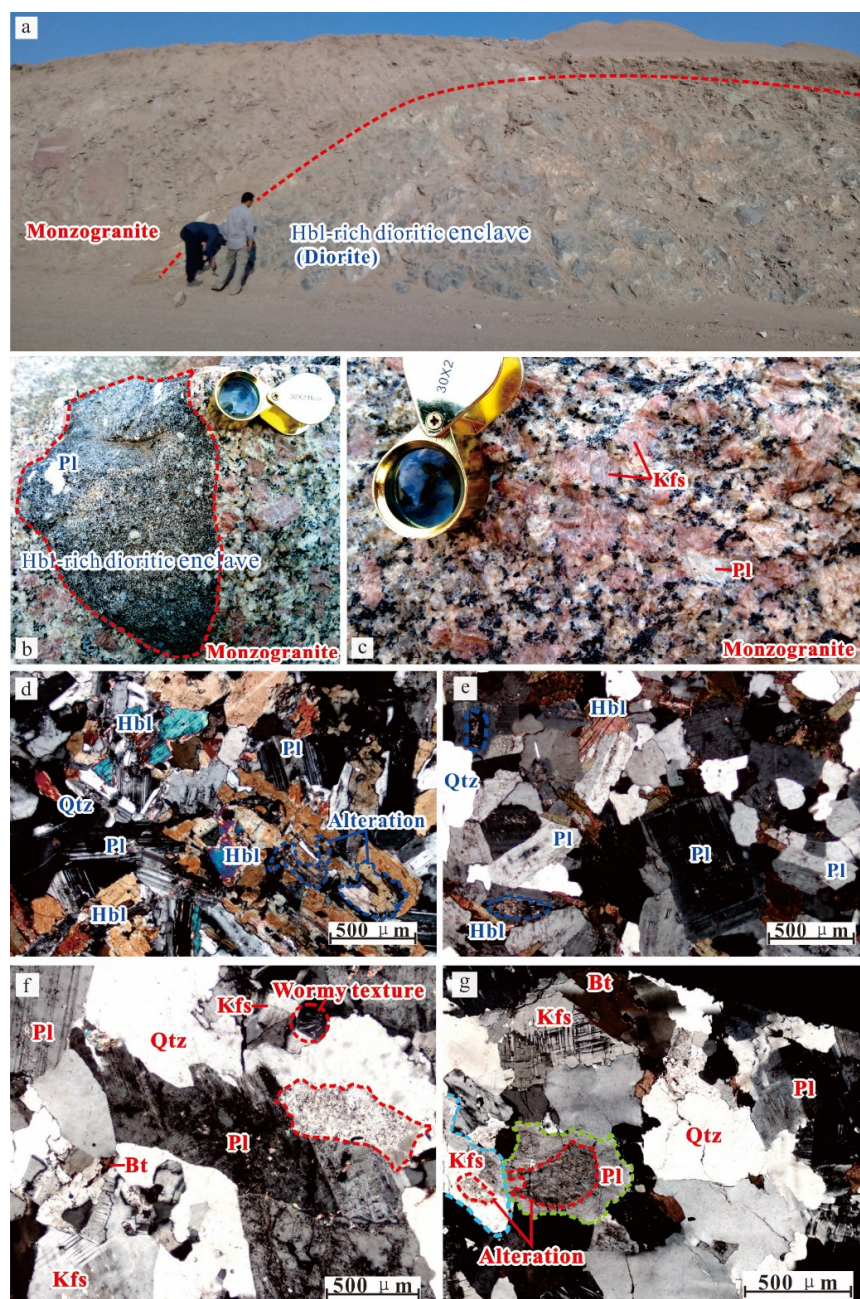


**Figure 3.** Field observations and photomicrographs. (a) Outcrop of Hbl-rich dioritic enclaves (diorite) and monzogranite. (b) Field relationships of the Hbl-rich dioritic enclaves. (c) Macroscopic view of monzogranite. (d,e) Photomicrographs of diorite. (f,g) Photomicrographs of monzogranite. Pl, plagioclase; Kfs, K-feldspar; Hbl, hornblende; Qtz, quartz; Bt, biotite.

The medium-to-coarse-grained monzogranite samples are gray-white to light-red, the latter due to a high K-feldspar content (Figure 3a–c). Constituent minerals include ~40% quartz, 20%–25% plagioclase, 25%–30% alkali feldspar, 5%–10% biotite, 2%–3% hornblende, and accessory minerals of zircon and magnetite (Figure 3f,g). The plagioclase crystals range in size from 0.5 to 5 mm, are typically dark gray, and subhedral, with plate-prismatic shapes, and some crystals have undergone intensive sericitization and kaolinization. The plagioclase crystals have a wormy texture and perfect cleavages. The alkali feldspar crystals are 0.2–8 mm, are composed of K-feldspar and microcline, and are light gray and subhedral, with plate-prismatic shapes. Cleavage in the K-feldspar is sparse, with some intensively altered simple twins. Crosshatch twinning is evident in the microcline crystals. The granular quartz allotriomorphic grains are generally greater than 0.5 mm in size, with alteration-related embayments along the grain edges, with undulatory extinction. The <1 mm biotite crystals are widely dispersed in the rock. The hornblende grains are small in size, with observed chloritization and carbonation caused by alteration. Accessory minerals occupy interstitial mineral spaces.

### 3. Methods

#### 3.1. LA-ICP-MS Zircon Analyses

Zircon selection was performed by Chengpu Geological Testing Co., Ltd., Langfang, China, and cathode luminescence photographs were obtained at the State Key Laboratory of Geological Processes and Mineral Resources, China University of Geosciences, Wuhan. An analytical scanning electron microscope (JSM-IT100) connected to a GATAN MINICL system captured sample images at 10.0–13.0 kV and 80–85  $\mu$ A, using a tungsten filament.

#### 3.2. Zircon U-Pb Ages

U-Pb radiometric dating and zircon trace element composition were simultaneously measured by LA-ICP-MS at the Wuhan Sample Solution Analytical Technology Co., Ltd., Wuhan, China. Laser sampling was performed using a GeolasPro laser ablation system consisting of a 193 nm wavelength COMPexPro 102ArF excimer laser beam with maximum energy of 200 mJ, in a MicroLas optical system. An Agilent 7700e ICP-MS instrument was used to acquire in-signal intensities. Helium and argon were used as carrier and make-up gases, respectively, mixed via a T-connector before injection into the ICP. Signal smoothing was performed by incorporating a “wire” signal smoothing device with the laser ablation system [43]. Laser spot size and frequency were set to 30  $\mu$ m and 5 Hz, respectively. Zircon 91500 and glass NIST610 were used as external standards for U-Pb dating and trace element calibration, respectively. Each analysis incorporated approximately 20–30 s background acquisition, followed by 50 s data collection. An Excel-based software package ICPMSDataCal 12 was used to perform off-line selection and integration of background and analyzed signal data, time-drift correction, and quantitative calibration for trace element analysis and U-Pb dating [44,45]. Concordia diagrams and weighted mean calculations were made using Isoplot/Ex\_ver3 [46].

#### 3.3. Lu-Hf Isotopes

In situ Hf isotope data was collected with a Neptune Plus MC-ICP-MS (Thermo Fisher Scientific, Germany), in combination with a Geolas HD excimer ArF laser ablation system (Coherent, Göttingen, Germany) at the Wuhan Sample Solution Analytical Technology Co., Ltd., Wuhan, China. The laser ablation system was fitted with a “wire” signal smoothing device to correct the signal at low laser repetition rates of 1 Hz [47]. Helium served as a carrier gas within the ablation cell and argon as make-up gas after leaving the ablation cell. Small amounts of nitrogen were added to the argon make-up gas flow to improve

the sensitivity for acquiring Hf isotopes [48]. Compared to the standard arrangement, the addition of nitrogen in combination with the use of the newly designed X skimmer cone and Jet sample cone in the Neptune Plus improved the signal intensity for Hf, Yb, and Lu by a factor of 5.3, 4.0, and 2.4, respectively. Zircon analysis data were obtained in single-spot ablation mode with a 44  $\mu\text{m}$  spot size and with a laser ablation energy density of  $\sim 7.0 \text{ J cm}^{-2}$  for 20 s for background analysis and 50 s of ablation for data acquisition. Detailed operating conditions for the laser ablation system, the MC-ICP-MS instrument, and data analysis are as described by Hu, Liu [48].

A major limitation for accurate in situ zircon Hf isotope determination by LA-MC-ICP-MS was the very large isobaric interference from  $^{176}\text{Yb}$ , and to a much lesser extent,  $^{176}\text{Lu}$  on  $^{176}\text{Hf}$ . It has been shown that the mass fractionation of Yb ( $\beta\text{Yb}$ ) is inconsistent over time and that the  $\beta\text{Yb}$  that is obtained from the introduction of solutions is unsuitable for in situ zircon measurements [49]. Under- or over-estimation of the  $\beta\text{Yb}$  value undoubtedly affects the accuracy of the correction for  $^{176}\text{Yb}$ , and thus the determined  $^{176}\text{Hf}/^{177}\text{Hf}$  ratio. We applied the directly obtained  $\beta\text{Yb}$  value from the zircon sample itself in real-time and the  $^{179}\text{Hf}/^{177}\text{Hf}$  and  $^{173}\text{Yb}/^{171}\text{Yb}$  ratios used to calculate the mass bias of Hf ( $\beta\text{Hf}$ ) and Yb ( $\beta\text{Yb}$ ). This was normalized to  $^{179}\text{Hf}/^{177}\text{Hf} = 0.7325$  and  $^{173}\text{Yb}/^{171}\text{Yb} = 1.132685$  [50] using an exponential correction function for mass bias. Interference of  $^{176}\text{Yb}$  on  $^{176}\text{Hf}$  was corrected by measuring the interference-free  $^{173}\text{Yb}$  isotope and the  $^{176}\text{Yb}/^{173}\text{Yb}$  ratio of 0.79639 [50] used to calculate the  $^{176}\text{Yb}/^{177}\text{Hf}$  ratio. Similarly, the relatively minor interference of  $^{176}\text{Lu}$  on  $^{176}\text{Hf}$  was corrected by measuring the intensity of the interference-free  $^{175}\text{Lu}$  isotope and then using the recommended  $^{176}\text{Lu}/^{175}\text{Lu}$  ratio of 0.02656 [51] to calculate the  $^{176}\text{Lu}/^{177}\text{Hf}$  ratio. We used the mass bias of Yb ( $\beta\text{Yb}$ ) to calculate the mass fractionation of Lu, as they have similar physicochemical properties. Off-line selection and integration of sample signals and mass bias calibrations were performed using the aforementioned ICPMSDataCal software package (Ver 12) [44].

### 3.4. Whole-Rock Geochemistry

Preliminarily processing of fresh samples was carried out at the Geological Survey Institute, China University of Geosciences, Wuhan. Samples were crushed into a powder, so grain sizes were  $<75 \mu\text{m}$ , at the State Key Laboratory of Biogeology and Environmental Geology, China University of Geosciences, Wuhan. Care was taken during the preparation of the powder to eliminate possible contamination from other sources. Major and trace element analyses were carried out at ALS Minerals–ALS Chemex, Guangzhou, China. Whole-rock major element concentrations were determined by initial acid digestion in lithium borate and subsequent X-ray fluorescence (ME-XRF26d), with errors being less than 1%. Trace element and rare earth element concentrations were determined by initial mixed acid digestion, followed by plasma mass spectrometry (M61-MS81). The mantle-normalized, multi-element spider diagrams; chondrite-normalized, rare-earth element patterns; and other diagrams were constructed using Geokitfre software (Ver. build20250725) [52].

## 4. Results

### 4.1. Zircon U-Pb Ages

Twenty selected zircons were analyzed for U-Pb ages by LA-ICP-MS from the Hbl-rich diorite and twenty from the monzogranite. The grains consisted of long euhedral 100–300  $\mu\text{m}$  columnar crystals, with 1.2–4.0 length–width ratios. The yellowish-brown crystals mostly exhibited primary oscillatory zoning, with a few depicting faint and flaky zoning. The most notable differences between the zircons extracted from the two rock types was a wider to more flaky zonation for the Hbl-rich diorite zircons, while the monzogranite zircons were characterized by finer oscillatory zoning. In addition, the zircons from the



monzogranite typically have inherited cores (Figure 4a,c). The zircons generally have high Th and U concentrations with correspondingly high  $^{232}\text{Th}/^{238}\text{U}$  ratios (Figure 4e), while their associated U-Pb data are listed in Table S1. The mineral texture, rare earth element (REE) contents, and Th/U ratios are shown in Figure 4e,f.

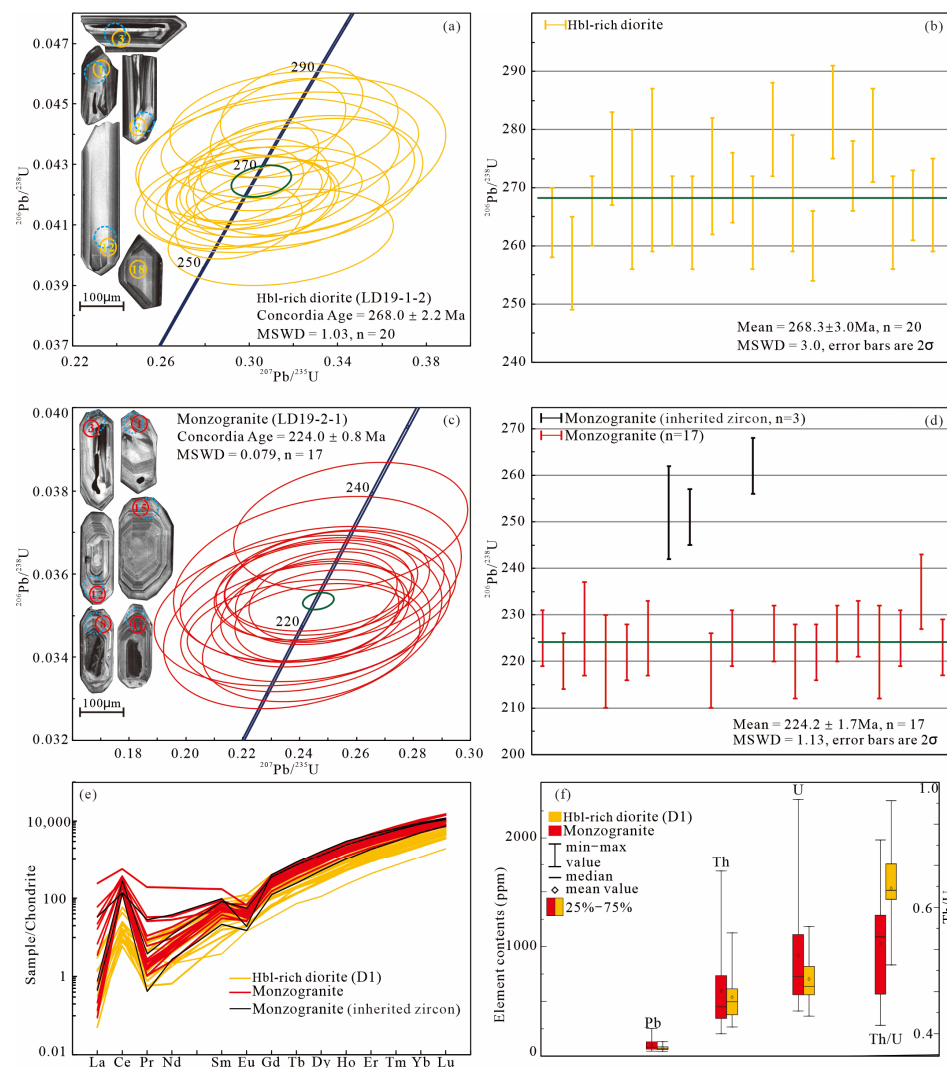


**Figure 4.** (a) CL images and concordant ages of the Hbl-rich diorite; (b) concordant age and weighted average age of the Hbl-rich diorite; (c) CL images and concordant age of the monzogranite; (d) concordant age and weighted average age of the monzogranite; (e) the chondrite-normalized REE diagrams of zircon for the Hbl-rich diorite and monzogranite (after Sun and McDonough [53]); (f) the Pb, Th, and U element compositions of zircon for Hbl-rich diorite and monzogranite.

Zircon Th and U concentrations of 255–1114 ppm and 354–1172 ppm, respectively, for the diorite, had associated Th/U ratios of 0.56–0.95. Concordant data greater than 97% generated spot clustering near the concordant curve in the  $^{206}\text{Pb}/^{238}\text{U}$ - $^{207}\text{Pb}/^{235}\text{U}$  diagram. The estimated concordant age for the Hbl-rich diorite was  $268.0 \pm 2.2$  Ma with a mean square weighted deviation (MSWD = 1.03;  $n = 20$ ; Figure 4a). The  $^{206}\text{Pb}/^{238}\text{U}$  ages ranged from 257 to 283 Ma, with a weighted average of  $268.3 \pm 3.0$  Ma (MSWD = 3.0;  $n = 20$ , Figure 4b). Thus, a middle Permian formation age is inferred for the Hbl-rich diorite rocks, with overlapping (i.e., within their respective error ranges) concordant and weighted average ages.

Most zircon  $^{206}\text{Pb}/^{238}\text{U}$  ratios from the monzogranite gave ages spread between 218 and 235 Ma, with a weighted average of  $224.2 \pm 1.7$  Ma and a MSWD = 1.13 as  $n = 17$

(Figure 4d). Those with ages of 252–262 Ma, obtained from LD19-2-7, LD19-2-8, and LD19-2-11 samples, indicate that these Permian zircon grains were inherited. Except for these three inherited zircon grains, Th and U contents range from 194 to 1679 ppm and 390 to 2341 ppm, respectively, with corresponding Th/U ratios of 0.41–0.86. Similarly, the concordant data greater than 97% for the monzogranites revealed an age of  $224.0 \pm 0.8$  Ma with MSWD = 0.079, as  $n = 17$  (Figure 4c). These two mutually supportive ages indicate that the monzogranite formed in the Late Triassic.

## 4.2. Whole-Rock Geochemistry

### 4.2.1. Hbl-Rich Diorite

Whole-rock major and trace element concentrations for five Hbl-rich diorite samples are listed in Table S2, with corresponding loss-on-ignition [54] values of 0.91–1.75 wt.% indicating slight hydrothermal alteration of the rock.

Major element compositions for the Hbl-rich diorite are characterized by a low 53.68–59.14 ( $\bar{x} = 56.25$  wt.%) of  $\text{SiO}_2$  and 0.95–2.96 wt.% of  $\text{K}_2\text{O}$ , with  $\text{K}_2\text{O}/\text{Na}_2\text{O}$  ratios of 0.25–0.61 and a high  $\text{Na}_2\text{O}$  content of 3.63–4.98 wt.%. Corresponding  $\text{Al}_2\text{O}_3$  concentrations range from 16.95 to 17.70 wt.%; with  $\text{MgO}$ , 2.26 to 5.41 wt.%;  $\text{FeO}_T$ , 5.81 to 9.75 wt.%;  $\text{CaO}$ , 3.38 to 8.48 wt.%;  $\text{MnO}$ , 0.11 to 0.15 wt.%; and  $\text{TiO}_2$ , 0.88 to 1.55 wt.% (Figure 5) and  $\text{Mg}^\#$  values of 49–60. Moderate total alkali ( $\text{K}_2\text{O} + \text{Na}_2\text{O}$ ) concentration in the diorite coincides with low alkaline ratios (ARs) of 1.42–2.18 wt.%, while A/NK and A/CNK ratios of 1.57–2.53 and 0.79–1.01, respectively, point to moderate enrichment on the aluminum saturation index. Thus, the Hbl-rich diorite magmatic series are calc-alkaline, metaluminous, and moderately enriched in potassium and are magnesian-rich on an Fe-index scheme (Figure 6).

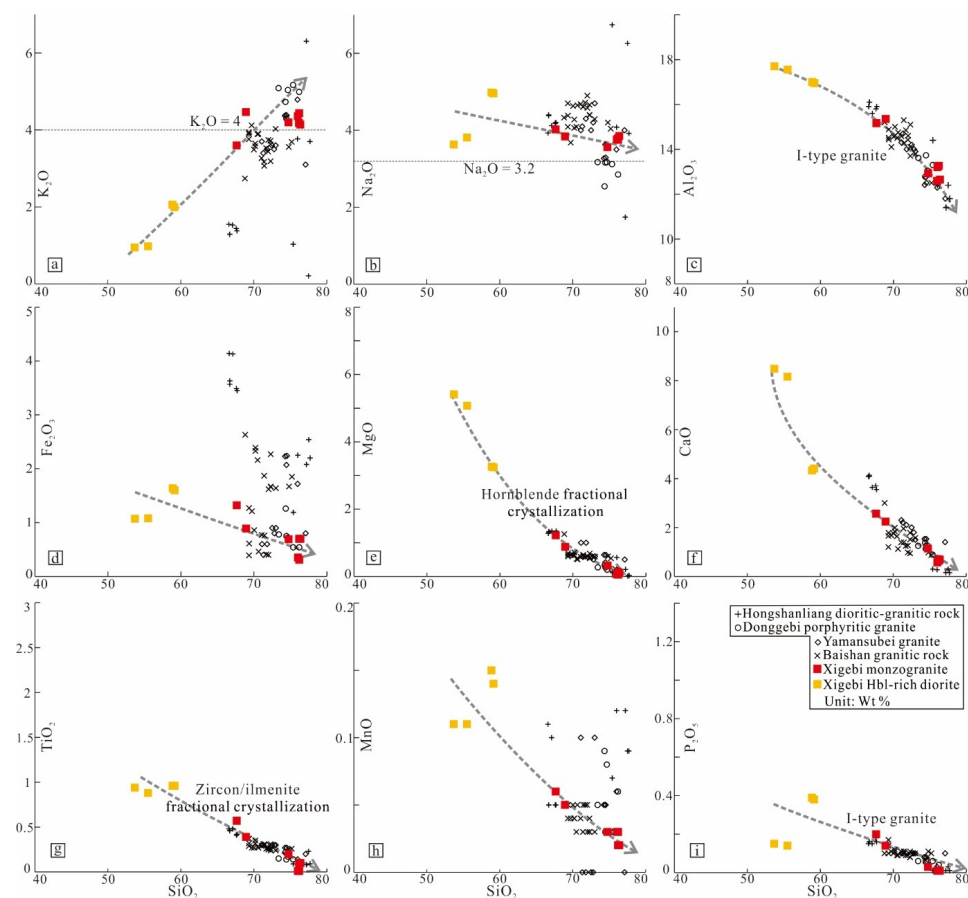


**Figure 5.** Harker diagrams: (a)  $\text{K}_2\text{O}$ - $\text{SiO}_2$ , (b)  $\text{Na}_2\text{O}$ - $\text{SiO}_2$ , (c)  $\text{Al}_2\text{O}_3$ - $\text{SiO}_2$ , (d)  $\text{Fe}_2\text{O}_3$ - $\text{SiO}_2$ , (e)  $\text{MgO}$ - $\text{SiO}_2$ , (f)  $\text{CaO}$ - $\text{SiO}_2$ , (g)  $\text{TiO}_2$ - $\text{SiO}_2$ , (h)  $\text{MnO}$ - $\text{SiO}_2$ , and (i)  $\text{P}_2\text{O}_5$ - $\text{SiO}_2$ .



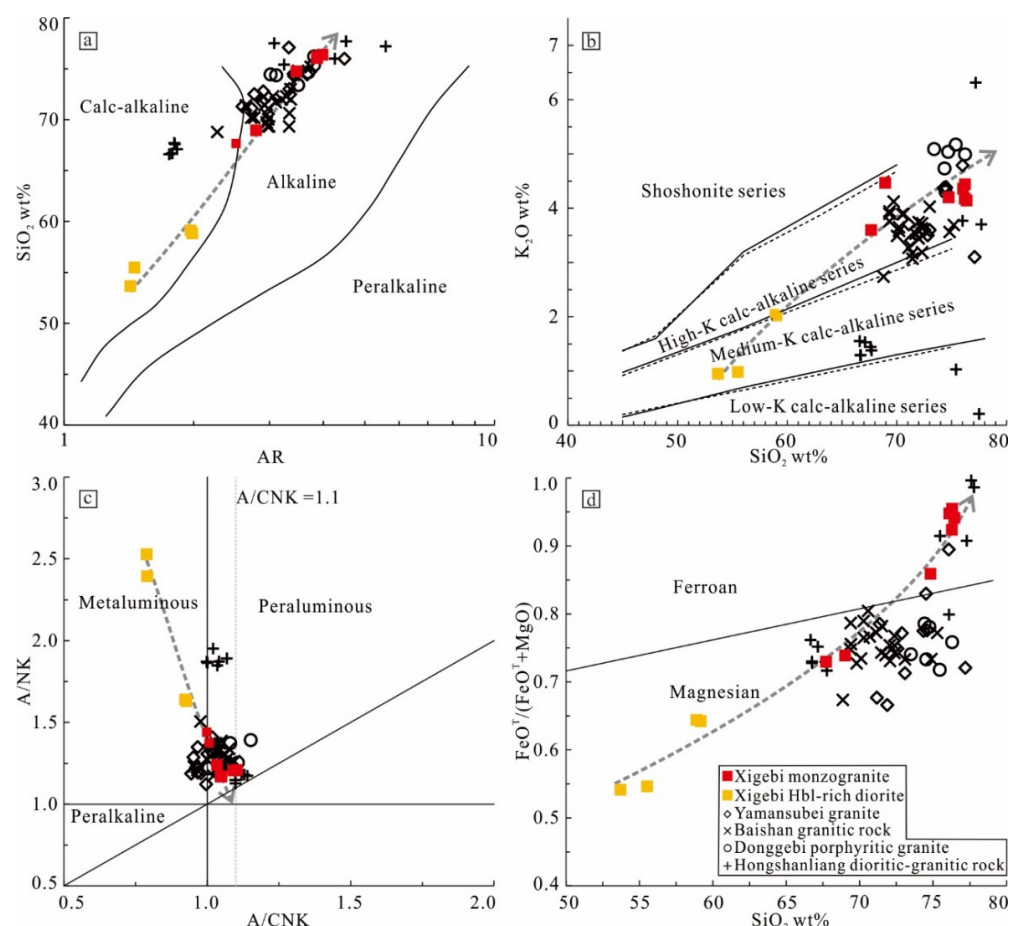


**Figure 6.** Geochemical discrimination diagrams for the Hbl-rich diorite and monzogranite. (a)  $\text{Na}_2\text{O} + \text{K}_2\text{O}$ - $\text{SiO}_2$  (after Wright [55]), (b)  $\text{K}_2\text{O}$ - $\text{SiO}_2$  (after Peccerillo and Taylor [56]), (c)  $\text{A/NK}$ - $\text{A/CNK}$  (after Maniar and Piccoli [57]), (d)  $\text{Fe}$ -index- $\text{SiO}_2$  (after Frost, Barnes [58]).  $\text{AR} = (\text{Al}_2\text{O}_3 + \text{CaO} + \text{Na}_2\text{O} + \text{K}_2\text{O})/(\text{Al}_2\text{O}_3 + \text{CaO} - \text{Na}_2\text{O} - \text{K}_2\text{O})$  (wt.%);  $\text{A/NK} = \text{Al}_2\text{O}_3/(\text{Na}_2\text{O} + \text{K}_2\text{O})$  molar;  $\text{A/CNK} = \text{Al}_2\text{O}_3/(\text{CaO} + \text{Na}_2\text{O} + \text{K}_2\text{O})$  molar.

The total REE concentration abundances are moderate, ranging from 68.60 to 136.13 ppm. Two samples display values lower than 100 ppm, because of lower light REE (LREE) concentrations. These two samples also have higher MgO and CaO concentrations but lower levels of  $\text{K}_2\text{O}$  and total alkalis. The concentration of LREEs and HREEs spanned 54.09–128.34 ppm and 7.49–14.56 ppm, respectively, and corresponding LREE/HREE ratios,  $(\text{La}/\text{Yb})_{\text{N}}$ , and  $\delta \text{Eu}$  concentrations of 3.71–16.83, 3.29–21.86, and 0.95–1.01, respectively. REE distributions exhibit high levels of LREEs with strong differentiation. The concentration of LILEs (e.g., Rb, K, and Pb) and the HFSE Th are enriched compared to typical primitive mantle compositions. However, all the Hbl-rich diorite samples are depleted in the HFSEs Nb, Ti, and Eu (Figure 7).

With regards to the trace element compositions, sample LD19-0-2 exhibited a significant deviation from the other Hbl-rich diorites. The HREEs and trace elements and low  $\text{Sr}/\text{Y}$  and  $\text{La}/\text{Yb}$  ratios may reflect alteration processes with respect to sample LD19-0-2. The obvious negative Eu anomaly is consistent with plagioclase fractionation and alteration (Figure 7). Thus, we suggest that this sample is not representative of the Hbl-rich diorite but is included in the dataset for reference.

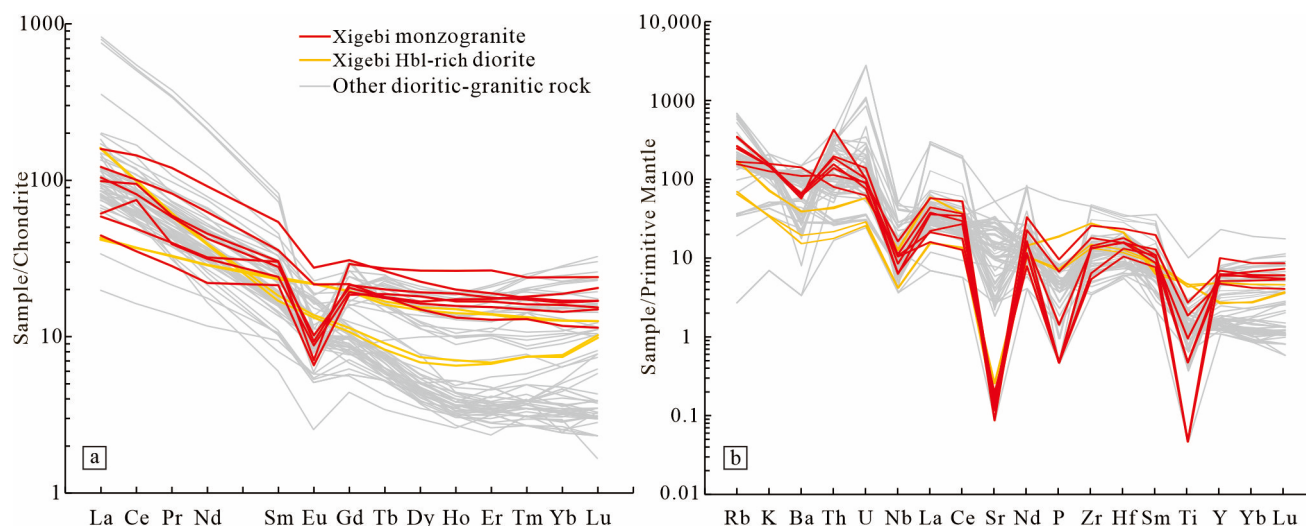


**Figure 7.** Diagrams for chondrite-normalized REEs (a) and primitive mantle (b) for the Hbl-rich diorite and monzogranite in the Xigezi area. The other sources and lithologies plotted are for comparative purposes and after Sun and McDonough [53].

#### 4.2.2. Monzogranite

Table S2 contains geochemical data for seven analyzed monzogranite samples which have LOI values of 0.30–0.70 wt.%. Major element concentrations are relatively high, with  $\text{SiO}_2$  between 67.65 and 76.37 wt.% ( $\bar{x} = 73.73$  wt.%), 3.60 and 4.47 wt.% for  $\text{K}_2\text{O}$ , and 7.62 and 8.31 wt.% for the total alkali ( $\text{K}_2\text{O} + \text{Na}_2\text{O}$ ) content (Figure 5). Their  $\text{K}_2\text{O}/\text{Na}_2\text{O}$  ratios are between 0.89 and 1.18 (with six samples having ratios greater than 1.07) but are characterized by low  $\text{Al}_2\text{O}_3$  values of 12.65–15.35 wt.% (Figure 5). They contain 0.02–0.06 wt.% of  $\text{MgO}$ ,  $\text{FeO}_T$  of 1.05–3.29 wt.% (five samples having values < 2.00 wt.%), 0.57–2.56 wt.% for  $\text{CaO}$  (five samples being < 1.15 wt.%), 0.01–0.57 wt.% for  $\text{TiO}_2$ , and 0.02–0.06 wt.% for  $\text{MnO}$  (Figure 5). The monzogranite samples have relatively high alkaline ratios of 2.50–3.98, a slightly elevated aluminum saturation index characterized by  $A/NK = 1.09$ –1.44 and  $A/CNK = 0.90$ –1.10, and low  $\text{Mg}^\#$  values of 7–39. High-K calc-alkaline, peraluminous, and general ferroan magmatic series are therefore characteristics of the monzogranites (Figure 6).

Total REEs concentrations range from 65 to 211 ppm, due mainly to variable LREEs content, with four samples having concentrations > 121 ppm. The LREEs and HREEs concentrations span 48.63–189.88 ppm and 14.39–24.91 ppm, respectively, with corresponding LREE/HREE ratios of 2.71–9.32,  $(\text{La}/\text{Yb})_N$  ratios of 2.44–10.38, and  $\delta \text{Eu}$  values ranging from 0.24 to 0.77. REE concentrations exhibit strong differentiation, marked by enrichment in LREEs and relatively stable HREE concentrations. The monzogranites exhibit negative Eu anomalies and low  $\text{Sr}/\text{Y}$  and  $\text{La}/\text{Yb}$  ratios. They are enriched in the HFSEs Th and Hf but depleted in Nb, Ti, and Eu. The LILEs, Ba and Sr, remain relatively low compared to neighboring elements (Figure 7).

The concentration of major elements in both the Hbl-rich diorite and monzogranite rocks, and various dioritic-granitic rocks in eastern Tianshan, display distinct fractionation trends on Harker diagrams (Figure 5). In the Xigezi pluton, the monzogranite has higher K concentrations but lower Al, Mg, Ca, Ti, and Mn values than the Hbl-rich diorite (Figure 5). In addition, there is a significant increase in K and a slight increase in the  $A/CNK$  ratio and the level of iron-magnesium saturation with increasing Si. However, the Xigezi Hbl-rich diorite shows a visible difference in K content, total alkalis, and Al concentrations in relation to the Xigezi monzogranite and the other magmatic rocks (Figure 6). The total REE concentrations of the Xigezi monzogranite and Weiya syenogranite are nevertheless similar, with overall LREE/HREE ratios that are lower than for the Xigezi Hbl-rich diorites

and the Weiya granodiorites. However, the Xigebi rocks are composed of lower La, Ce, Sr, and Nd concentrations than the Weiya rocks but are more enriched in Ba, Y, Yb, and Lu concentrations (Figure 7).

#### 4.2.3. Zircon Lu-Hf Isotopes

The Lu-Hf isotope data ( $n = 15$ ; Table S3) is characterized by positive  $\varepsilon_{\text{Hf}}(t)$  values for both the Hbl-rich diorite and monzogranite samples (Figure 8). Although the monzogranite exhibits lower  $\varepsilon_{\text{Hf}}(t)$  values and older model ages than the Hbl-rich diorite.

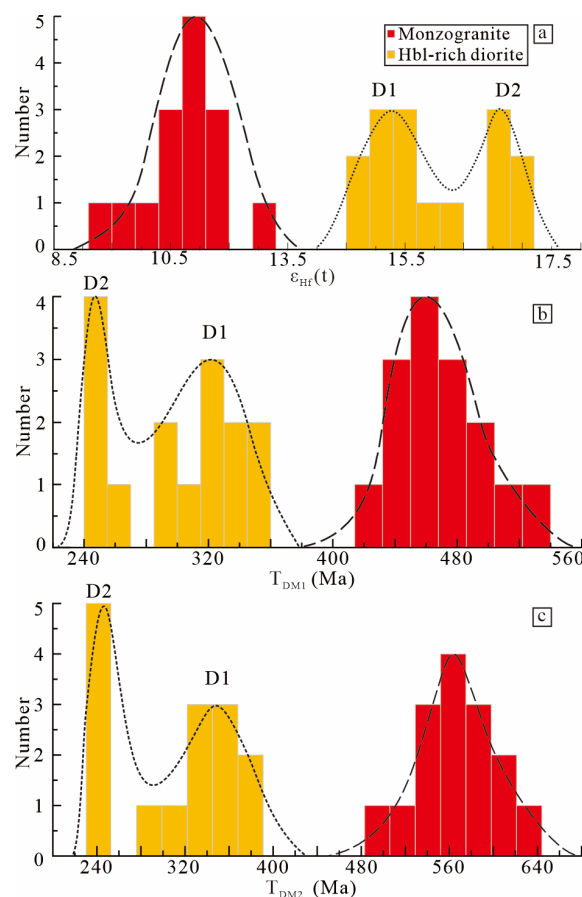


**Figure 8.** The Lu-Hf isotope data plotted on a histogram. (a) Histogram for  $\varepsilon_{\text{Hf}}(t)$ , (b) histogram for  $T_{\text{DM1}}$ , (c) histogram for  $T_{\text{DM2}}$ .

The Lu-Hf isotopes for the Hbl-rich diorite can be divided into two groups; Group D1, which encompasses most samples, has  $^{176}\text{Hf}/^{177}\text{Hf}$  ratios ranging from 0.2830005 to 0.283046, while the ratios for Group D2 span 0.283069–0.283086. Group D1 has  $^{176}\text{Lu}/^{177}\text{Hf}$  ratios from 0.000405 to 0.001516, with corresponding  $\varepsilon_{\text{Hf}}(t)$  values of 14.0–15.5. Group D2 has  $^{176}\text{Lu}/^{177}\text{Hf}$  ratios from 0.000820 to 0.001919, with  $\varepsilon_{\text{Hf}}(t)$  values of 16.3–16.7. The  $T_{\text{DM1}}$  for D1 (287.5–348.5 Ma;  $\bar{x} = 323.6$  Ma) is greater than the corresponding U-Pb ages for the rock, while  $T_{\text{DM2}}$  ranges from 295.6 to 380.8 Ma with a mean of 345.9 Ma. The  $T_{\text{DM2}}$  value of 380.8 Ma gave a minimum value for  $\varepsilon_{\text{Hf}}(t)$  of 14.0 (Figure 8). There was no obvious difference in the  $T_{\text{DM1}}$  and  $T_{\text{DM2}}$  values for Group D2, with both being close to the U-Pb ages for the rock.

The  $^{176}\text{Hf}/^{177}\text{Hf}$  ratios for the monzogranite are between 0.282881 and 0.282957, with corresponding  $^{176}\text{Lu}/^{177}\text{Hf}$  ratios between 0.000530 and 0.001259 and  $\varepsilon_{\text{Hf}}(t)$  values of 8.7–11.3. The  $T_{\text{DM1}}$  416.5–524.0 Ma values ( $\bar{x} = 470.3$  Ma) are greater than the U-Pb ages for the monzogranite. The  $T_{\text{DM2}}$  values span 493.0–643.8 Ma ( $\bar{x} = 568.4$  Ma), with a  $T_{\text{DM2}}$  value of 643.8 Ma which gives a minimum  $\varepsilon_{\text{Hf}}(t)$  value of 8.7 (Figure 8).

## 5. Discussion

### 5.1. Petrogenesis

Granitic rocks can form by the partial melting of continental crust or by magmatic crystallization and mixing processes which may occur in regions such as at the lithosphere/crust boundary [59,60]. However, some researchers insist that granites are only generated from the melting of crustal material rather than from lithospheric sources [61]. The petrogenesis of the Hbl-rich diorite and monzogranite rocks are discussed below, using the S, I, M, and A-type granites (“SIMA”) scheme, which uses a combination of field, mineral, and geochemical criteria [54,60,62]. Because this four-type SIMA classification scheme typically associates S-type granites with metasedimentary source rocks, A-type with anorogenic provenance, I-type with metaigneous protolith, and M-type with mantle source origin, it enables evaluating the petrogenesis of the dioritic and monzogranitic lithologies with respect to source, magmatic evolution, emplacement dynamics, and tectonic setting. Particularly, distinguishing the source regions for the Hbl-rich diorite and monzogranite is important for pinning down formation mechanism, structure, and crustal reworking processes associated with the study interval across the eastern Tianshan region.

#### 5.1.1. Hbl-Rich Diorite

The Hbl-rich diorite has lower whole-rock  $Mg^\#$  than primitive mantle melts and has high saturation temperatures of zircons ( $\sim 737\text{--}799^\circ\text{C}$ , [63–65], indicating the parental magma was generated in the deep crust. The rocks are characterized by low incompatible element concentrations, including low  $SiO_2$ ,  $K_2O$  (Figure 5a), AR (Figure 6a) and  $FeO^T/(FeO^T + MgO)$  ratios of 0.54–0.78 (Figure 6d), and high  $TiO_2$  and  $MnO$  values (Figure 5g,h). Their 10,000 Ga/Al ratios of 2.17–2.81 are less than expected for A-type granites (Figure 9a,b) which typically have ratios of  $\sim 3.75$  [66], while the 187.40–372.6 values for  $Zr + Nb + Ce + Y$  are close to the boundary for A-type granites and unfractionated M-, I- and S-type granites (Figure 9c). When taken together, the dataset points to no A-type granitic association for the diorite. Moreover, the low 0.79–1.01 A/CNK and the mostly  $>1$  A/NK ratios (Figure 6c) distinctly characterize metaluminous granites [57,60,67]. The diorites contain significant amounts of biotite, as well as hornblende, and have high LREE concentrations, but depleted in Al-rich minerals like muscovite and HREEs. Combined with their low A/CNK ratios, this observation suggests that the Hbl-rich diorite is affiliated to I-type granite-like metaluminous middle-high-K calc-alkaline rocks (Figure 6; Douce [68], Skjerlie and Dana [69]).

These calc-alkaline I-type granites could have been generated by three primary petrological processes [70–73]: (1) early fractional crystallization and cumulation derived from cogenetic magmas [74,75]; (2) partial melting of igneous rocks such as basalts or metabasalts [76,77]; and (3) mixing of crust-derived and mantle-derived magmas [78,79].

The low  $Mg^\#$  together with high Rb/Sr ratios ( $>0.5$ ) indicate that the diorite may have been generated from the melting of a crustal source. This suggests that the high  $\epsilon_{Hf}(t)$  values (Figure 8) were a consequence of melting juvenile crust, or due to the magma mixing with mantle material [80]. Although, both the Lu-Hf isotopes and model ages (Figure 8) point towards the involvement of a juvenile crustal component. Some samples have high Nb/Ta ratios  $> 14.4$  [81] (Figure 10a), elevated Zr/Hf ratios of 41.47–46.61 compared to primitive mantle values of 37 [53],  $Mg^\#$  values  $> 45$  [82], and D2 zircon compositions typical of a mantle source characterized by high  $\epsilon_{Hf}(t)$  values; all consistent with mantle material mixing with partial melts from a juvenile crustal component. The diorite has low  $SiO_2$ , Sr, Sr/Y and Th/La ratios (Figure 11c,d), moderate to high  $Na_2O/K_2O$  ratios, high  $Al_2O_3$ , enriched in LREEs but depleted in HREEs, consistent with rocks formed by partial melting of meta-basalt [83]. The presence of two distinct zircons might also be a consequence of



magma mixing. Thus, the composition of the Hbl-rich diorite was dominated by the melting of basaltic juvenile lower crust which was mixed with mantle-derived magma [84–89].

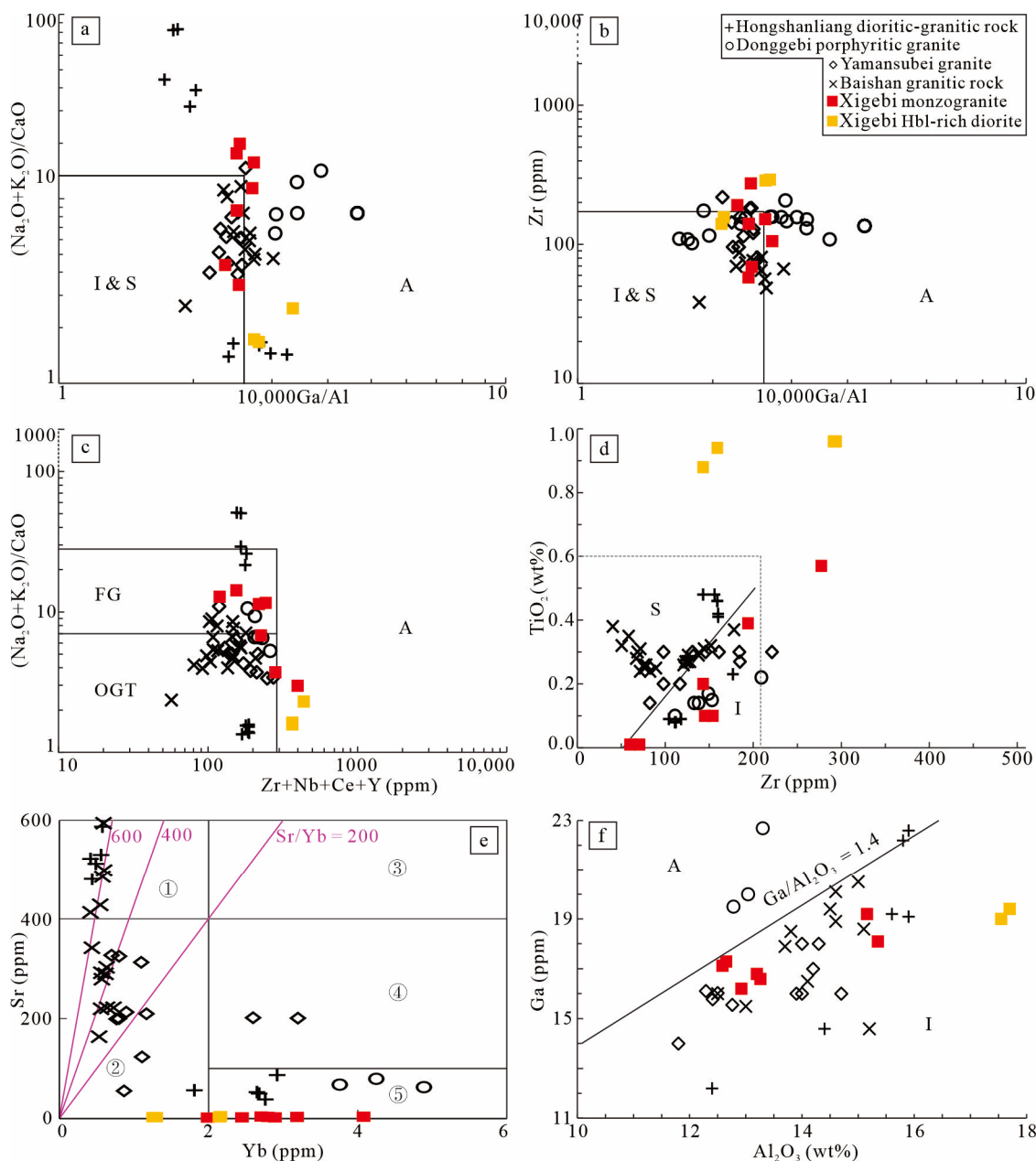


**Figure 9.** Discrimination diagrams for granite rock types. (a)  $\text{K}_2\text{O} + \text{Na}_2\text{O}/\text{CaO}$ - $10,000 \text{ Ga}/\text{Al}$ . (b)  $\text{Zr}$ - $10,000 \text{ Ga}/\text{Al}$ . (c)  $(\text{K}_2\text{O} + \text{Na}_2\text{O})/(\text{CaO}-\text{Zr} + \text{Nb} + \text{Ce} + \text{Y})$  ((a–c) after Whalen, Currie [66]). (d)  $\text{TiO}_2$ -Zr. I, I-type granites. S, S-type granites. A, A-type granites. FG, felsic granites. OGT, unfractionated M-, I-, and S-type granites. ①, High Sr and low Yb contents. ②, Low Sr and low Yb contents. ③, High Sr and high Yb contents. ④, Extremely low Sr and high Yb contents. ⑤, Low Sr and high Yb contents.

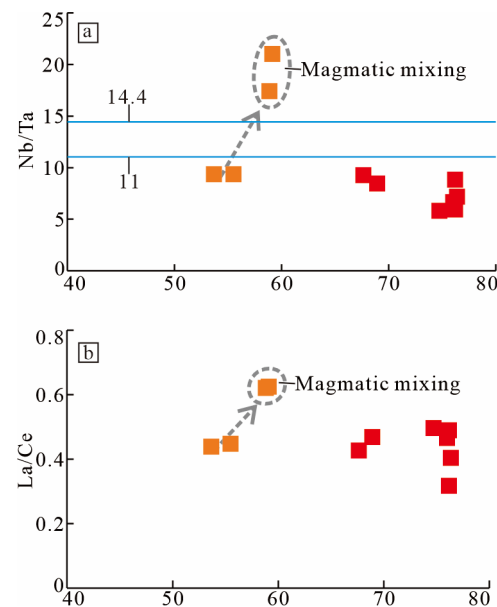


**Figure 10.** Geochemical contents for different magmatic sources. (a) Nb/Ta-SiO<sub>2</sub>, (b) La/Ce-SiO<sub>2</sub>.

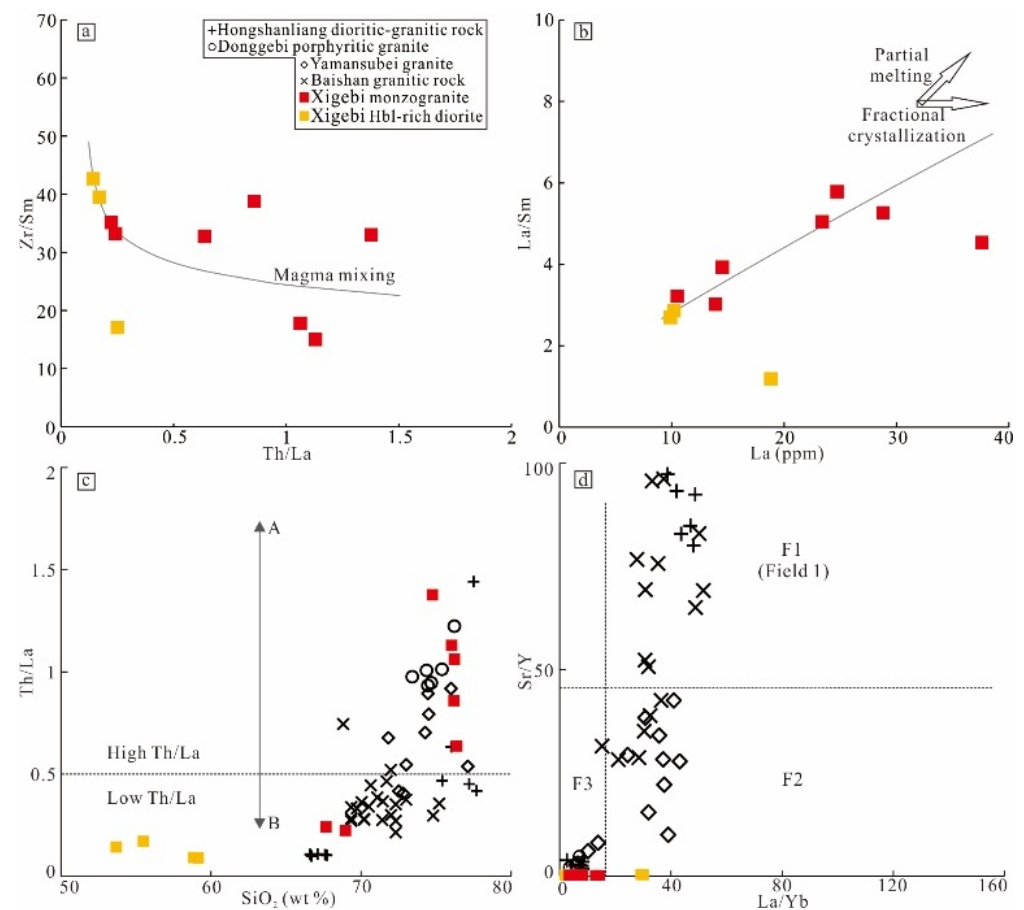


**Figure 11.** Geochemical diagrams for magmatic sources and different evolutionary pathways. (a) Zr/Sm-Th/La. (b) La/Sm-La. (c) Th/La-SiO<sub>2</sub>. High Th/La ratios in magmatic rocks indicate relatively large contributions from sedimentary source rocks. 'A' indicates partial melting of sediment-dominated crustal sources and 'B', partial melting of mafic crustal sources. (d) Sr/Y-La/Yb. Adakitic melts were derived from eclogitic rocks in the garnet stability field, with little or no plagioclase (F1). Crustal melts in the stability field for both plagioclase and garnet (F2). Crustal melts in the stability field for plagioclase, with little or no garnet present (F3). (a,b) after Du, Long [41]; (c,d) after Wang, Xue [26].

### 5.1.2. Monzogranite

The monzogranite has high  $\text{SiO}_2$ ,  $\text{K}_2\text{O}$  (Figure 5a), total alkali concentrations, and  $\text{K}_2\text{O}/\text{Na}_2\text{O}$  ratios and moderate-to-high zircon saturation temperatures ( $T = 704\text{--}838\text{ }^\circ\text{C}$ ). They are further characterized by low  $\text{MgO}$ ,  $\text{CaO}$ ,  $\text{TiO}_2$ , and  $\text{MnO}$  concentrations (Figure 5e–h), together with high AR (Figure 6a) and moderate-to-high  $\text{FeO}^T/(\text{FeO}^T + \text{MgO})$  ratios of 0.72–0.95 (Figure 6d). Importantly, their chemical composition is similar to contemporary dioritic-granitic rocks in eastern Tianshan (Figure 5). However, unlike A-type granites, the 10,000 Ga/Al ratios of the monzogranites are notably lower, ranging from 2.36 to 2.74, with low  $\text{Zr} + \text{Nb} + \text{Ce} + \text{Y}$  values of 114.20–404.70 (Figure 9a–c). The high biotite content further indicates that the source magma was hydrous rather than anhydrous. These results are not consistent with what would be expected for a typical A-type granite [57,60]. The monzogranites also lack features typical of S-type granites, as they do not contain Al-rich minerals and have low A/CNK ratios of 0.90–1.10 (Figure 6c), flat HREEs, high Yb values, and uncharacteristic LREE concentrations (Figure 7; [60,67]). Rather, the major (Figure 5c,i) and trace (Figure 7) element concentrations and high LREE/HREE ratios are more like those of peraluminous, high-K calc-alkaline to alkaline I-type granites (Figures 6 and 9).

The low  $\text{MgO}$ ,  $\text{CaO}$ ,  $\text{TiO}_2$ , and  $\text{MnO}$  values, elevated  $\text{SiO}_2$ ,  $\text{K}_2\text{O}$ , total alkalis, iron, REEs, and trace element content, combined with the Lu-Hf isotopic systematics, are distinct from the Hbl-rich dioritic enclaves. This indicates that the diorite and monzogranite have different primary origins, rather than simply reflecting different levels of fractional crystallization and cumulation during a prolonged period of magmatism. The high  $\text{SiO}_2$  content, Zr/Hf ratios of 17–41 (with five samples having Zr/Hf ratios close to average continental crust) [80], moderate-to-high Th/La ratios (Figure 11c), low  $\text{Mg}^\#$  values of <45, and low Nb/Ta ratios of 11 (Figure 10a) are inconsistent with magma from the mantle that simply underwent late-stage fractional crystallization [93,94], when we consider that samples, which were also depleted in Eu and Nb, had low Sr/Y, La/Ce, and La/Yb ratios, but were enriched in Hf, pointed towards a deep crustal partial melting origin for the monzogranite (Figures 10b and 11).

Overall, the geochemical results rule out a metasedimentary source rock. For example, the low  $\text{Mg}^\#$  ratios are more consistent with partial melting of a deep crustal meta-basaltic protolith [83]. The  $\varepsilon_{\text{Hf}}(t)_{(\text{granite})}$  values of 8.7–11.3 and model ages further link them to the melting of juvenile crust, while the high Th/La ratios (Figure 11b) and peraluminous nature of the rocks are consistent with potential contamination by shallow metasedimentary rocks. Thus, it is proposed that the monzogranitic magma was dominated by the melting of deep crustal meta-basalts. The presence of plagioclase phenocrysts, slight-to-moderately negative Eu anomalies, and low Sr/Y and La/Yb ratios (Figure 11d) could be attributed to early fractional crystallization of plagioclase during the partial melting of crustal material.

### 5.2. Multiple-Stage Magmatism During Juvenile Crustal Reworking

The Hbl-rich diorite has greater  $\varepsilon_{\text{Hf}}(t)$  values but lower  $T_{\text{DM1}}$  and  $T_{\text{DM2}}$  compositions than the monzogranite (Figure 8). These observations are consistent with a scenario whereby the diorite was emplaced into the middle Permian crust as a somewhat primitive magma but was later captured by the host monzogranite magma during a later Triassic upwelling event, indicating multiple stages of magmatism in the eastern Tianshan area. That is consistent with the relations of mineralogical characteristics (Figure 3), geochemical signatures (Figures 4 and 10), and Lu-Hf isotopic characteristics (Figures 8 and 12).

A period of post-collisional tectonics commenced sometime in the late Permian [19,31,95–106], accompanied by several episodes of magmatic evolution in eastern Tianshan (Figure 13). In the Jueluotage belt, multiple depositional intervals are evident in the sedimentary sequences, including well-developed Carboniferous continental sediments in the Jueluotage

Belt. Pelagic sediments formed in the southern Jueluotage Belt and are marked by continental braided, shallow riverine lacustrine detrital sediments intercalated with lenticular limestone bodies, while the Jurassic and Cenozoic continental sediments collectively record the transition from a continental margin depositional regime to an intraplate, intermontane, depositional regime. In addition, the cessation of sedimentary deposition at certain periods geographically indicates that eastern Tianshan was not a persistently stable basin from the late Paleozoic to Mesozoic, thus needing more evidence to further constrain the within-plate evolution.

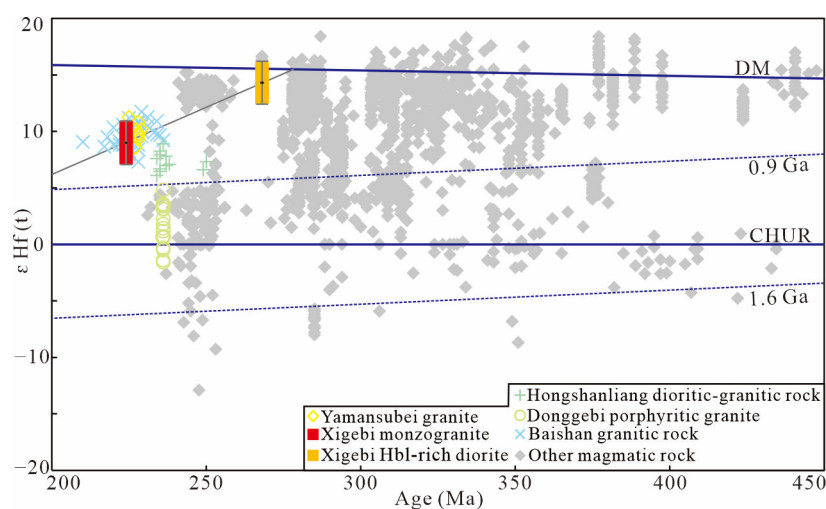


**Figure 12.** Hf isotope evolution diagram.

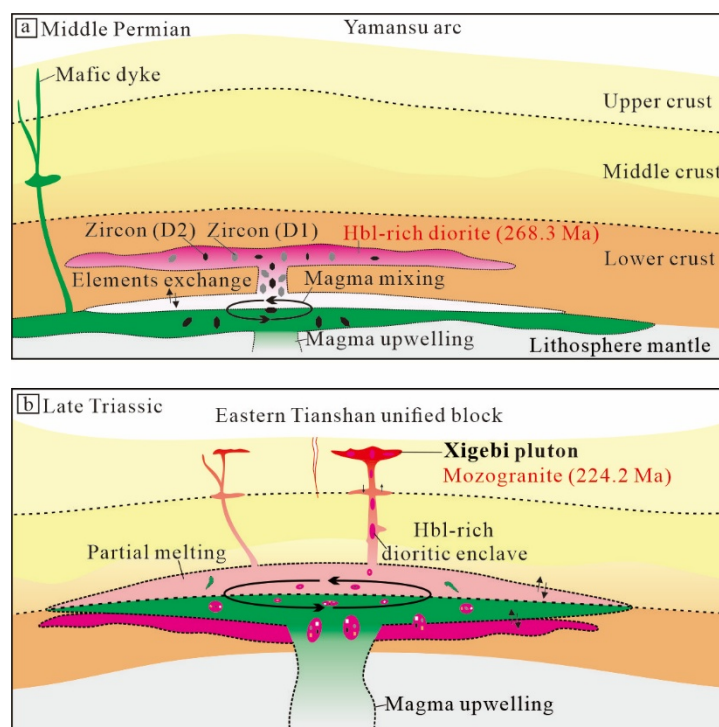


**Figure 13.** Schematic diagrams showing crustal reworking processes from the middle Permian to the late Triassic (no scale). (a) Middle Permian intrusive Hbl-rich diorite in a post-collisional setting. (b) Late Triassic monzogranite generated and captured the Hbl-rich dioritic enclaves during asthenospheric underplating and mixing in intraplate setting, with the continental crust consequently being thinned.



This study denotes that both the 268 Ma Hbl-rich diorite and the 224 Ma monzogranite were generated by magma underplating in a post-collisional and intraplate setting. In addition, the  $T_{DM1}$  and high  $\epsilon_{Hf}(t)$  values (Figures 8 and 12) are consistent with a model involving juvenile crust (Figure 13), indicating widespread reworking of the juvenile crust by magmatism. The data suggest that only a short interval of magmatism ensued since ca. 268 Ma, that is between the post-collisional and intraplate stages, which points to the absence of continuous magmatic activity since the Permian period. The crustal thickening and thinning caused by magma underplating resulted in the recycling of lower crustal material and emplacement in the upper crust. This continuous exchange of material and tectonic activity is suggested to have been widespread but intermittent.

Based on the tectonic evolution of eastern Tianshan, it is proposed that there were three stages of juvenile crustal reworking, marked by (1) melting of a subduction-modified block due to asthenospheric upwelling, resulting in the generation of basic rocks, (2) lower crustal accretion and crustal thickening, with partial melting of the lower crust which contained the remains of island arc residual material, which generated the Hbl-rich diorites (appinite-like) and bimodal volcanic rocks (Figure 13a), and (3) partial melting of a juvenile crust dominated by large-scale upwelling of magma from the mantle, accompanied by significant thinning of the crust. The magmatism also underwent mixing processes and contamination with shallow metasedimentary strata. This produced the characteristic intraplate rocks such as the monzogranite which contained the older Hbl-rich dioritic enclaves (Figures 3 and 13b).

### 5.3. Geological Implications

The Xigebi pluton is located on the Jueluotage Belt, which together with the Bogeda–Haerlike Belt and the Middle Tianshan Terrane lies between the Junggar Basin in the north and the Tarim Craton in the south (Figure 1). Together, this assemblage makes up a crucial part of the southern margin of the CAOB [1–6,8,28,29,107]. A review on the origin of the Kanggur Ocean and a number of small branched oceanic basins in eastern Tianshan infer that the basins closed by the Permian [31]. Field relationships show that a  $280.2 \pm 1.4$  Ma undeformed granite in the Kanggur area intruded a  $283.7 \pm 2.4$  Ma mylonized rock which was affected by early ductile shear deformation via thrusting. This seems to limit the early N-S extensional coaxial ductile deformation to a relatively short period from 290 to 280 Ma, which represents the time the Kanggur Ocean closed [108]. In agreement with the work presented here, a detailed study by Feng and Zheng [21] on magmatism from the Weiya intrusive complex, from the Middle Tianshan Terrane, concluded that the complex formed in an intracontinental setting during the Triassic. Moreover, the Permian to Triassic magmatism from the Bogeda–Haerlike Belt shows that, although the area had undergone subduction in the Carboniferous, it had changed to a post-collisional extensional setting with further transformation to an intraplate environment [21,31,107]. A variety of research now indicates that the Jueluotage, Bogeda–Haerlike belts, and the Middle Tianshan Terrane shared a similar tectonic environment to eastern Tianshan, consistent with sedimentary record. Consequently, eastern Tianshan and the southern part of eastern Junggar experienced moderate-to-rapid cooling of their basements in the Cretaceous [109]. This study provides a mechanistic explanation that contributes towards the validation of the above proposition.

In this model, the ophiolitic mélanges in eastern Tianshan are thought to represent multiple oceanic and continental arc stages [31,96,98,110]. Further, previous studies have compared eastern Tianshan with the Beishan Orogenic Belt [2,9,10], where magmatism and the terrane composition in eastern Tianshan and the Beishan Belt indicate widespread regional tectonic activity in NW China, associated with W-E oriented extension and crustal

thinning [2,9,10,111]. The Triassic magmatic events indicate a wide regional period of extension in the eastern Tianshan area, on the southern margin of the CAO. Consequently, the magmatic upwelling and crustal thinning played a significant role with regards to forming geological deposits in the eastern Tianshan area.

## 6. Conclusions

The Xigebi pluton consists of Hbl-rich diorite and monzogranite which crystallized at  $268.3 \pm 3.0$  Ma and  $224.2 \pm 1.7$  Ma, respectively. The former was subsequently captured by the monzogranite as enclaves. With distinct magmatic sources, the diorite originated from the melting of lower crustal meta-igneous rocks, which was mixed with melts from the mantle. The monzogranite source was dominated by deep crustal meta-basalts, with evidence for contamination by shallow metasedimentary rocks. There was likely some mixing between this melt with deeply sourced magma from the mantle. The continental crust in eastern Tianshan was vertically stratified, with magmatic underplating events in eastern Tianshan recording multiple stages of juvenile crustal reworking, when the tectonic environment shifted from a post-collisional to an intraplate setting. The post-collisional stage ended prior to ca. 270 Ma and the intraplate extensional stage started before ca. 250 Ma. The Triassic magmatism in eastern Tianshan is likely related to the widespread concurrent regional extension that was happening across NW China on the southern margin of the CAO. It represents a critical juncture in the terminal tectonic evolution of the CAO. The magmatic upwelling and crustal thinning were likely significant in producing geological deposits across eastern Tianshan.

**Supplementary Materials:** The following supporting information can be downloaded at <https://www.mdpi.com/article/10.3390/min15080829/s1>, Table S1: zircon LA-ICP-MS U-Pb data of monzogranite (LD19-2-1) and granodiorite (LD19-1-2); Table S2: whole rock geochemistry results of monzogranite and granodiorite samples; Table S3: Lu-Hf isotopes of monzogranite (LD19-2-1) and granodiorite (LD19-1-2); Table S4: compilation of age data for Devonian-Triassic intrusive rocks in the eastern Tianshan.

**Author Contributions:** Conceptualization, W.Z. and H.L.; methodology, W.Z.; formal analysis, H.L.; investigation, M.M.; resources, M.W.; data curation, W.Z.; writing—original draft preparation, M.W., W.Z. and H.L.; writing—review and editing, E.C.F. and T.S.; visualization, H.L.; supervision, W.Z.; project administration, W.Z.; funding acquisition, M.W. All authors have read and agreed to the published version of the manuscript.

**Funding:** This research was funded by the China Geological Survey (No. DD20179607, DD20160060).

**Data Availability Statement:** The original contributions presented in this study are included in the article/Supplementary Material. Further inquiries can be directed to the corresponding author.

**Acknowledgments:** We would like to thank the editors and reviewers for their constructive comments. We would also like to use this opportunity to thank those researchers that assisted with field investigations and sampling.

**Conflicts of Interest:** Author Mahemuti Muredili was employed by the PetroChina Xinjiang Oilfield Company. The remaining authors declare that the research was conducted in the absence of any commercial or financial relationships that could be construed as a potential conflict of interest.

## References

1. Li, W.Y. The primary discussion on the relationship between Paleo-Asian Ocean and Paleo-Tethys Ocean. *Acta Petrol. Sin.* **2018**, *34*, 2201–2210.
2. Windley, B.F.; Alexeev, D.; Xiao, W.J.; Kroener, A.; Badarch, G. Tectonic models for accretion of the Central Asian Orogenic Belt. *J. Geol. Soc.* **2007**, *164*, 31–47. [[CrossRef](#)]

3. Xu, Z.Q.; Li, S.T.; Zhang, J.X.; Yang, J.S.; He, B.Z.; Li, H.B.; Lin, C.S.; Cai, Z.H. Paleo-Asian and Tethyan tectonic systems with docking the Tarim block. *Acta Petrol. Sin.* **2011**, *27*, 1–22.
4. Dobretsov, N.L.; Buslov, M.M.; Vernikovskiy, V.A. Neoproterozoic to Early Ordovician evolution of the Paleo-Asian Ocean: Implications to the break-up of Rodinia. *Gondwana Res.* **2003**, *6*, 143–159. [\[CrossRef\]](#)
5. Zhao, G.C.; Cawood, P.A. Precambrian geology of China. *Precambrian Res.* **2012**, *222*, 13–54. [\[CrossRef\]](#)
6. Li, Y.B.; Li, H.Q.; Zhou, W.X.; Wang, B.; Chang, F.; Li, S.C.; Yang, X.J. Neoproterozoic thermal events and tectonic implications in the Beishan orogenic belt: Geochemical and geochronological evidence from two sets of granitic rocks from southern Beishan orogenic belt, Gansu Province. *Geol. Bull. China* **2021**, *40*, 1117–1139.
7. Stern, R.J.; Li, S.M.; Keller, G.R. Continental crust of China: A brief guide for the perplexed. *Earth-Sci. Rev.* **2018**, *179*, 72–94. [\[CrossRef\]](#)
8. Li, J.; Wu, C.; Chen, X.H.; Zuza, A.V.; Haproff, P.J.; Yin, A.; Shao, Z.G. Tectonic evolution of the Beishan orogen in central Asia: Subduction, accretion, and continent-continent collision during the closure of the Paleo-Asian Ocean. *GSA Bull.* **2022**, *135*, 819–851. [\[CrossRef\]](#)
9. Xiao, W.J.; Mao, Q.G.; Windley, B.F.; Han, C.M.; Qu, J.F.; Zhang, J.E.; Ao, S.J.; Guo, Q.Q.; Cleven, N.R.; Lin, S.F.; et al. Paleozoic multiple accretionary and collisional processes of the Beishan orogenic collage. *Am. J. Sci.* **2010**, *310*, 1553–1594. [\[CrossRef\]](#)
10. Xiao, W.J.; Zhang, L.C.; Qin, K.Z.; Sun, S.; Li, J.L. Paleozoic accretionary and collisional tectonics of the Eastern Tianshan (China): Implications for the continental growth of Central Asia. *Am. J. Sci.* **2004**, *304*, 370–395. [\[CrossRef\]](#)
11. Chen, F.Y.; Wang, B.; Li, H.Q.; Chang, F. Zircon U-Pb geochronology, geochemistry and tectonic significance of the Peraluminous intrusive rocks in the Borenaobao-Bayanmende area, Xilinhot, Inner Mongolia. *Miner. Explor.* **2019**, *10*, 768–780.
12. Deng, Y.F.; Yuan, F.; Hollings, P.; Song, X.Y.; Zhou, T.f.; Fu, B.; Denysyn, S.; Zhao, B.b. Magma generation and sulfide saturation of Permian mafic-ultramafic intrusions from the western part of the Northern Tianshan in NW China: Implications for Ni-Cu mineralization. *Miner. Depos.* **2020**, *55*, 515–534. [\[CrossRef\]](#)
13. Feng, W.Y.; Zhu, Y.F. Petrogenesis and tectonic implications of the late Carboniferous calc-alkaline and shoshonitic magmatic rocks in the Awulale mountain, western Tianshan. *Gondwana Res.* **2019**, *76*, 44–61. [\[CrossRef\]](#)
14. Li, D.D.; Wang, Y.W.; Shi, Y.; Xie, H.J.; Wang, J.B.; Lai, C. Age and geochemistry of the Carboniferous-Permian magmatism and Fe-Ti-V oxide metallogeny in the Eastern Tianshan Orogen, NW China: Evidence from the Yaxi mafic-ultramafic complex. *Int. Geol. Rev.* **2019**, *61*, 853–867. [\[CrossRef\]](#)
15. Su, B.X.; Qin, K.Z.; Sakyi, P.A.; Li, X.H.; Yang, Y.H.; Sun, H.; Tang, D.M.; Liu, P.P.; Xiao, Q.H.; Malaviarachchi, S.P.K. U-Pb ages and Hf-O isotopes of zircons from Late Paleozoic mafic-ultramafic units in the southern Central Asian Orogenic Belt: Tectonic implications and evidence for an Early-Permian mantle plume. *Gondwana Res.* **2011**, *20*, 516–531. [\[CrossRef\]](#)
16. Zhao, L.D.; Chen, H.Y.; Hollings, P.; Han, J.S. Late Paleozoic magmatism and metallogenesis in the Agishan-Yamansu belt, Eastern Tianshan: Constraints from the Bailingshan intrusive complex. *Gondwana Res.* **2019**, *65*, 68–85. [\[CrossRef\]](#)
17. Liu, H.F.; Zhao, H.; Guo, R.L.; Wang, G.C.; Liao, Q.A. Geochronology, geochemistry and geological implications of Early Carboniferous A-type granites in Harlik area from the Eastern Tianshan. *Earth Sci.* **2022**, *47*, 2245–2263.
18. Zhou, W.X.; Zhao, X.C.; Lü, X.B. Petrology, Geochemistry and Chronology of the Baishahe Formation in Numohong Area of Eastern Kunlun Orogenic Belt. *Earth Sci.* **2020**, *45*, 4370–4388.
19. Yang, H.; Xiao, W.; Mao, Q.; An, S.; Bai, Y.; Sang, M.; Cai, H.; Li, H. Two episodes of extension induced by slab rollback and root foundering in the Eastern Tianshan, southwestern Altaids: Insights from granites and intermediate dykes. *Lithos* **2024**, *476–477*, 107616. [\[CrossRef\]](#)
20. Gao, F.; Cheng, Y.; Guo, R.; Liu, X.; Liu, Z. The Late Carboniferous Mafic-Ultramafic Complex Induced by Slab Breakoff in Eastern North Tianshan, Central Asian Orogenic Belt. *Minerals* **2023**, *13*, 1293. [\[CrossRef\]](#)
21. Feng, W.Y.; Zheng, J.H. Triassic magmatism and tectonic setting of the eastern Tianshan, NW China: Constraints from the Weiya intrusive complex. *Lithos* **2021**, *394*, 106171. [\[CrossRef\]](#)
22. Mao, Q.G.; Ao, S.J.; Windley, B.F.; Wang, J.B.; Li, Y.C.; Xiao, W.J. Middle Triassic lower crust-derived adakitic magmatism: Thickening of the Dananhu intra-oceanic arc and its implications for arc-arc amalgamation in the Eastern Tianshan (NW China). *Geol. J.* **2021**, *56*, 3137–3154. [\[CrossRef\]](#)
23. Lei, R.X.; Wu, C.Z.; Zhang, Z.Z.; Gu, L.X.; Tang, J.H.; Li, G.R. Geochronology, geochemistry and tectonic significances of the Yamansubei pluton in eastern Tianshan, Northwest China. *Acta Petrol. Sin.* **2013**, *29*, 2653–2664.
24. Zhang, X.R.; Zhao, G.C.; Sun, M.; Han, Y.G.; Liu, Q. Triassic magmatic reactivation in Eastern Tianshan, NW China: Evidence from geochemistry and zircon U-Pb-Hf isotopes of granites. *J. Asian Earth Sci.* **2017**, *145*, 446–459. [\[CrossRef\]](#)
25. Wu, Y.S.; Zhou, K.F.; Li, N.; Chen, Y.J. Zircon U-Pb dating and Sr-Nd-Pb-Hf isotopes of the ore-associated porphyry at the giant Donggebi Mo deposit, Eastern Tianshan, NW China. *Ore Geol. Rev.* **2017**, *81*, 794–807. [\[CrossRef\]](#)
26. Wang, Y.H.; Xue, C.J.; Liu, J.J.; Zhang, F.F. Geological, geochronological, geochemical, and Sr-Nd-O-Hf isotopic constraints on origins of intrusions associated with the Baishan porphyry Mo deposit in eastern Tianshan, NW China. *Miner. Depos.* **2016**, *51*, 953–969. [\[CrossRef\]](#)

27. Zhang, D.Y.; Zhou, T.F.; Yuan, F.; Xiao, W.J.; White, N.C.; Deng, Y.F.; Lu, W.W.; Deng, G. Petrogenesis and mineralization potential of a granite porphyry intrusion beneath the Baishan Mo deposit, Eastern Tianshan, NW China. *J. Asian Earth Sci.* **2015**, *113*, 254–265. [\[CrossRef\]](#)
28. Mao, Q.G.; Xiao, W.J.; Buckman, S.; Huang, P.; Ao, S.J.; Song, D.F.; Zhang, J.e.; Sang, M.; Tan, Z.; Wang, H.; et al. Deformational History of the Kanguer Subduction Complex in the Eastern Tianshan (NW China): Implications for Paleozoic-Triassic Multiple Accretionary Tectonics of the Southern Altaids. *Tectonics* **2022**, *41*, e2022TC007527. [\[CrossRef\]](#)
29. Zhao, T.Y.; Xiao, W.J.; Mao, Q.G.; Yang, H.; Abuduxun, N.; Li, P. The Wulanmoren Accretionary Complex unravels Early Devonian to Late Triassic multiple-arc amalgamation in the Tianshan Orogen (NW China). *Earth Space Sci.* **2023**, *10*, e2022EA002310. [\[CrossRef\]](#)
30. Li, N.; Yang, F.Q.; Zhang, Z.X.; Yang, C.D. Geochemistry and chronology of the biotite granite in the Xiaobaishitou W-(Mo) deposit, eastern Tianshan, China: Petrogenesis and tectonic implications. *Ore Geol. Rev.* **2019**, *107*, 999–1019. [\[CrossRef\]](#)
31. Wang, G.C.; Zhang, M.; Feng, J.L.; Liao, Q.A.; Zhang, X.H.; Kang, L.; Guo, R.L.; Xuan, Z.Y.; Han, K.Y. New understanding of the tectonic framework and evolution during the Neoproterozoic-Paleozoic era in the Eastern Tianshan Mountains. *J. Geomech.* **2019**, *25*, 798–819.
32. Chen, C.; Lv, X.B.; Wu, C.M.; Jiang, X.; Mao, C. Origin and Geodynamic Implications of Concealed Granite in Shadong Tungsten Deposit, Xinjiang, China: Zircon U-Pb Chronology, Geochemistry, and Sr-Nd-Hf Isotope Constraint. *J. Earth Sci.* **2018**, *29*, 114–129. [\[CrossRef\]](#)
33. Deng, X.H.; Chen, Y.J.; Santosh, M.; Wang, J.B.; Li, C.; Yue, S.W.; Zheng, Z.; Chen, H.J.; Tang, H.S.; Dong, L.H.; et al. U-Pb zircon, Re-Os molybdenite geochronology and Rb-Sr geochemistry from the Xiaobaishitou W-(Mo) deposit: Implications for Triassic tectonic setting in eastern Tianshan, NW China. *Ore Geol. Rev.* **2017**, *80*, 332–351. [\[CrossRef\]](#)
34. Liu, S.Y.; Wang, R.; Jeon, H.; Hou, Z.Q.; Xue, Q.w.; Zhou, L.M.; Chen, S.B.; Zhang, Z.L.; Xi, B.B. Indosinian magmatism and rare metal mineralization in East Tianshan orogenic belt: An example study of Jingerquan Li-Be-Nb-Ta pegmatite deposit. *Ore Geol. Rev.* **2020**, *116*, 103265. [\[CrossRef\]](#)
35. Sun, H.S.; Li, H.; Danisik, M.; Xia, Q.L.; Jiang, C.L.; Wu, P.; Yang, H.; Fan, Q.R.; Zhu, D.S. U-Pb and Re-Os geochronology and geochemistry of the Donggebi Mo deposit, Eastern Tianshan, NW China: Insights into mineralization and tectonic setting. *Ore Geol. Rev.* **2017**, *86*, 584–599. [\[CrossRef\]](#)
36. Zhang, Z.Z.; Gu, L.X.; Wu, C.Z.; Li, W.Q.; Xi, A.H.; Shuo, W. Zircon SHRIMP dating for the Weiya pluton, Eastern Tianshan: Its geological implications. *Acta Geol. Sin.-Engl. Ed.* **2005**, *79*, 481–490.
37. Wang, T.; Huang, H.; Zhang, J.; Wang, C.; Cao, G.; Xiao, W.; Yang, Q.; Bao, X. Voluminous continental growth of the Altaids and its control on metallogeny. *Natl. Sci. Rev.* **2022**, *10*, nwac283. [\[CrossRef\]](#)
38. Zhang, Z.Z.; Gu, L.X.; Wu, C.Z.; Zhai, J.P.; Li, W.Q.; Tang, J.H. Early Indosinian Weiya Gabbro in Eastern Tianshan, China: Elemental and Sr-Nd-O isotopic geochemistry, and its tectonic implications. *Acta Geol. Sin.-Engl. Ed.* **2007**, *81*, 424–432.
39. Zhang, Z.J.; Chen, H.Y.; Hu, M.Y.; Zhang, J.; Li, D.F. Isotopic geochemistry of the Jinwozi gold deposit in the eastern Tianshan orogen, NW China: Implications for the ore genesis. *Geol. J.* **2014**, *49*, 574–583. [\[CrossRef\]](#)
40. Zhao, L.D.; Chen, H.Y.; Hollings, P.; Han, J.S. Tectonic transition in the Aqishan-Yamansu belt, Eastern Tianshan: Constraints from the geochronology and geochemistry of Carboniferous and Triassic igneous rocks. *Lithos* **2019**, *344*, 247–264. [\[CrossRef\]](#)
41. Du, L.; Long, X.P.; Yuan, C.; Zhang, Y.Y.; Huang, Z.Y.; Wang, X.Y.; Yang, Y.H. Mantle contribution and tectonic transition in the Aqishan-Yamansu Belt, Eastern Tianshan, NW China: Insights from geochronology and geochemistry of Early Carboniferous to Early Permian felsic intrusions. *Lithos* **2018**, *304*, 230–244. [\[CrossRef\]](#)
42. Mao, Q.G.; Xiao, W.J.; Fang, T.H.; Windley, B.F.; Sun, M.; Ao, S.J.; Zhang, J.E.; Huang, X.K. Geochronology, geochemistry and petrogenesis of Early Permian alkaline magmatism in the Eastern Tianshan: Implications for tectonics of the Southern Altaids. *Lithos* **2014**, *190*, 37–51. [\[CrossRef\]](#)
43. Hu, Z.C.; Zhang, W.; Liu, Y.S.; Gao, S.; Li, M.; Zong, K.Q.; Chen, H.H.; Hu, S.H. “Wave” Signal-Smoothing and Mercury-Removing Device for Laser Ablation Quadrupole and Multiple Collector ICPMS Analysis: Application to Lead Isotope Analysis. *Anal. Chem.* **2015**, *87*, 1152–1157. [\[CrossRef\]](#)
44. Liu, Y.S.; Gao, S.; Hu, Z.C.; Gao, C.G.; Zong, K.Q.; Wang, D.B. Continental and Oceanic Crust Recycling-induced Melt-Peridotite Interactions in the Trans-North China Orogen: U-Pb Dating, Hf Isotopes and Trace Elements in Zircons from Mantle Xenoliths. *J. Petrol.* **2010**, *51*, 537–571. [\[CrossRef\]](#)
45. Liu, Y.S.; Hu, Z.C.; Gao, S.; Guenther, D.; Xu, J.; Gao, C.G.; Chen, H.H. In situ analysis of major and trace elements of anhydrous minerals by LA-ICP-MS without applying an internal standard. *Chem. Geol.* **2008**, *257*, 34–43. [\[CrossRef\]](#)
46. Ludwig, K.R. *ISOPLOT 3.00: A Geochronological Toolkit for Microsoft Excel*; Berkeley Geochronology Center: Berkeley, CA, USA, 2003; Volume 4, p. 39.
47. Hu, Z.C.; Liu, Y.S.; Gao, S.; Xiao, S.Q.; Zhao, L.S.; Guenther, D.; Li, M.; Zhang, W.; Zong, K.Q. A “wire” signal smoothing device for laser ablation inductively coupled plasma mass spectrometry analysis. *Spectrochim. Acta Part B-At. Spectrosc.* **2012**, *78*, 50–57. [\[CrossRef\]](#)



48. Hu, Z.C.; Liu, Y.S.; Gao, S.; Liu, W.G.; Zhang, W.; Tong, X.R.; Lin, L.; Zong, K.Q.; Li, M.; Chen, H.H.; et al. Improved in situ Hf isotope ratio analysis of zircon using newly designed X skimmer cone and jet sample cone in combination with the addition of nitrogen by laser ablation multiple collector ICP-MS. *J. Anal. At. Spectrom.* **2012**, *27*, 1391–1399. [\[CrossRef\]](#)
49. Woodhead, J.; Hergt, J.; Shelley, M.; Eggins, S.; Kemp, R. Zircon Hf-isotope analysis with an excimer laser, depth profiling, ablation of complex geometries, and concomitant age estimation. *Chem. Geol.* **2004**, *209*, 121–135. [\[CrossRef\]](#)
50. Fisher, C.M.; Vervoort, J.D.; Hanchar, J.M. Guidelines for reporting zircon Hf isotopic data by LA-MC-ICPMS and potential pitfalls in the interpretation of these data. *Chem. Geol.* **2014**, *363*, 125–133. [\[CrossRef\]](#)
51. Blichert-Toft, J.; Chauvel, C.; Albarede, F. Separation of Hf and Lu for high-precision isotope analysis of rock samples by magnetic sector multiple collector ICP-MS. *Contrib. Mineral. Petrol.* **1997**, *127*, 248–260. [\[CrossRef\]](#)
52. Lu, Y.F. Geokit—A geochemical toolkit for Microsoft Excel. *Geochimica* **2004**, *33*, 459–464.
53. Sun, S.S.; McDonough, W.E. Chemical and isotopic systematics of oceanic basalts: Implications for mantle composition and processes. *Geol. Soc. Lond. Spec. Publ.* **1989**, *42*, 313–345. [\[CrossRef\]](#)
54. Loiselle, M.C. Characteristics and origin of anorogenic granites. *Geol. Soc. America. Abstr. Programs* **1979**, *11*, 468.
55. Wright, J.B. A simple alkalinity ratio and its application to questions of non-orogenic granite genesis. *Geol. Mag.* **1969**, *106*, 370–384. [\[CrossRef\]](#)
56. Peccerillo, A.; Taylor, S.R. Geochemistry of eocene calc-alkaline volcanic rocks from the Kastamonu area, Northern Turkey. *Contrib. Mineral. Petrol.* **1976**, *58*, 63–81. [\[CrossRef\]](#)
57. Maniar, P.D.; Piccoli, P.M. Tectonic discrimination of granitoids. *Geol. Soc. Am. Bull.* **1989**, *101*, 635–643. [\[CrossRef\]](#)
58. Frost, B.R.; Barnes, C.G.; Collins, W.J.; Arculus, R.J.; Ellis, D.J.; Frost, C.D. A geochemical classification for granitic rocks. *J. Petrol.* **2001**, *42*, 2033–2048. [\[CrossRef\]](#)
59. Barbarin, B. A review of the relationships between granitoid types, their origins and their geodynamic environments. *Lithos* **1999**, *46*, 605–626. [\[CrossRef\]](#)
60. Chappell, B.W.; White, A.J.R. I-Type and S-Type Granites in the Lachlan Fold Belt. *Trans. R. Soc. Edinb.-Earth Sci.* **1992**, *83*, 1–26.
61. Zhang, Q.; Wang, Y.; Pan, G.Q.; Li, C.D.; Jin, W.J. Sources of granites: Some crucial questions on granite study (4). *Acta Petrol. Sin.* **2008**, *24*, 1193–1204.
62. Bonin, B. A-type granites and related rocks: Evolution of a concept, problems and prospects. *Lithos* **2007**, *97*, 1–29. [\[CrossRef\]](#)
63. Hanchar, J.M.; Watson, E.B. Zircon Saturation Thermometry. *Rev. Mineral. Geochem.* **2003**, *53*, 89–112. [\[CrossRef\]](#)
64. Anderson, D.L. Chemical composition of the mantle. *J. Geophys. Res. Solid Earth* **1983**, *88*, B41–B52. [\[CrossRef\]](#)
65. Hans Wedepohl, K. The composition of the continental crust. *Geochim. Cosmochim. Acta* **1995**, *59*, 1217–1232. [\[CrossRef\]](#)
66. Whalen, J.B.; Currie, K.L.; Chappell, B.W. A-type granites: Geochemical characteristics, discrimination and petrogenesis. *Contrib. Mineral. Petrol.* **1987**, *95*, 407–419. [\[CrossRef\]](#)
67. Chappell, B.W. Aluminum saturation in I- and S-type granites and the characterization of fractionated hapogranites. *Lithos* **1999**, *46*, 535–551. [\[CrossRef\]](#)
68. Douce, A.E.P. Generation of metaluminous A-type granites by low-pressure melting of calc-alkaline granitoids. *Geology* **1997**, *25*, 743–746. [\[CrossRef\]](#)
69. Skjerlie, K.P.; Dana, J.A. Fluid-Absent Melting Behavior of an F-Rich Tonalitic Gneiss at Mid-Crustal Pressures: Implications for the Generation of Anorogenic Granites. *J. Petrol.* **1993**, *34*, 785–815. [\[CrossRef\]](#)
70. Clemens, J.D. Granitic magmas with I-type affinities, from mainly metasedimentary sources: The Harcourt batholith of southeastern Australia. *Contrib. Mineral. Petrol.* **2018**, *173*, 93. [\[CrossRef\]](#)
71. Clemens, J.D.; Stevens, G.; Farina, F. The enigmatic sources of I-type granites: The peritectic connexion. *Lithos* **2011**, *126*, 174–181. [\[CrossRef\]](#)
72. Sisson, T.W.; Ratajeski, K.; Hankins, W.B.; Glazner, A.F. Voluminous granitic magmas from common basaltic sources. *Contrib. Mineral. Petrol.* **2005**, *148*, 635–661. [\[CrossRef\]](#)
73. Castro, A.; Morenoventas, I.; Delarosa, J.D. H-type (hybrid) granitoids: A proposed revision of the granite-type classification and nomenclature. *Earth Sci. Rev.* **1991**, *31*, 237–253. [\[CrossRef\]](#)
74. Defant, M.J.; Drummond, M.S. Derivation of some modern arc magmas by melting of young subducted lithosphere. *Nature* **1990**, *347*, 662–665. [\[CrossRef\]](#)
75. Cawthorn, R.G.; Strong, D.F.; Brown, P.A. Origin of corundum-normative intrusive and extrusive magmas. *Nature* **1976**, *259*, 102–104. [\[CrossRef\]](#)
76. Chappell, B.W. Compositional variation within granite suites of the Lachlan fold belt: Its causes and implications for the physical state of granite magma. *Trans. R. Soc. Edinb.-Earth Sci.* **1996**, *87*, 159–170.
77. Chappell, B.W.; White, A.J.R.; Wyborn, D. The importance of residual source material (restite) in granite petrogenesis. *J. Petrol.* **1987**, *28*, 1111–1138. [\[CrossRef\]](#)
78. Bonin, B. Do coeval mafic and felsic magmas in post-collisional to within-plate regimes necessarily imply two contrasting, mantle and crustal, sources? A review. *Lithos* **2004**, *78*, 1–24. [\[CrossRef\]](#)

79. Kocak, K.; Zedef, V.; Kansun, G. Magma mixing/mingling in the Eocene Horoz (Nigde) granitoids, Central southern Turkey: Evidence from mafic microgranular enclaves. *Mineral. Petrol.* **2011**, *103*, 149–167. [[CrossRef](#)]
80. Wu, F.Y.; Li, X.H.; Zheng, Y.F.; Gao, S. Lu-Hf isotopic systematics and their applications in petrology. *Acta Petrol. Sin.* **2007**, *23*, 185–220.
81. Taylor, S.R.; McLennan, B. *The Continental Crust: Its Composition and Evolution*; Blackwell Scientific Publications: Oxford, UK, 1985; p. 312.
82. Rapp, R.P.; Watson, E.B. Dehydration Melting of Metabasalt at 8–32 kbar: Implications for Continental Growth and Crust-Mantle Recycling. *J. Petrol.* **1995**, *36*, 891–931. [[CrossRef](#)]
83. Jung, S.; Hoernes, S.; Mezger, K. Synorogenic melting of mafic lower crust: Constraints from geochronology, petrology and Sr, Nd, Pb and O isotope geochemistry of quartz diorites (Damara orogen, Namibia). *Contrib. Mineral. Petrol.* **2002**, *143*, 551–566. [[CrossRef](#)]
84. Hibbard, M.J. Textural anatomy of twelve magma-mixed granitoid systems. *Enclaves Granite Petrol.* **1991**, *13*, 431–444.
85. Holden, P.; Halliday, A.N.; Stephens, W.E. Neodymium and strontium isotope content of microdiorite enclaves points to mantle input to granitoid production. *Nature* **1987**, *330*, 53–56. [[CrossRef](#)]
86. Vernon, R.H. Restite, xenoliths and microgranitoid enclaves in granites. *J. Proc. R. Soc. N. S. W.* **1983**, *116*, 77–103.
87. Wang, D.Z.; Zhou, X.M.; Xu, X.S.; Yao, Y.P. On geneses of microgranitoid enclaves. *J. Guilin Coll. Geol.* **1992**, *12*, 235–241.
88. Wang, D.Z.; Xie, L. Magma Mingling: Evidence from Enclaves. *Geol. J. China Univ.* **2008**, *14*, 16–21.
89. Roberts, M.P.; Clemens, J.D. Origin of high-potassium, calc-alkaline, I-type granitoids. *Geology* **1993**, *21*, 825. [[CrossRef](#)]
90. Zhang, Q.; Jin, W.J.; Li, C.D.; Wang, Y.L. Revisiting the new classification of granitic rocks based on whole-rock Sr and Yb contents: Index. *Acta Petrol. Sin.* **2010**, *26*, 985–1015.
91. Zhang, Q.; Jin, W.J.; Li, C.D.; Wang, Y.L. On the classification of granitic rock based on whole-rock Sr and Yb concentrations III. *Acta Petrol. Sin.* **2010**, *26*, 3431–3455.
92. Collins, W.J.; Beams, S.D.; White, A.J.R.; Chappell, B.W. Nature and origin of A-type granites with particular reference to southeastern Australia. *Contrib. Mineral. Petrol.* **1982**, *80*, 189–200. [[CrossRef](#)]
93. Ballouard, C.; Massuyeau, M.; Elburg, M.A.; Tappe, S.; Viljoen, F.; Brandenburg, J.-T. The magmatic and magmatic-hydrothermal evolution of felsic igneous rocks as seen through Nb-Ta geochemical fractionation, with implications for the origins of rare-metal mineralizations. *Earth-Sci. Rev.* **2020**, *203*, 103115. [[CrossRef](#)]
94. Ballouard, C.; Poujol, M.; Boulvais, P.; Branquet, Y.; Tartèse, R.; Vigneresse, J.-L. Nb-Ta fractionation in peraluminous granites: A marker of the magmatic-hydrothermal transition. *Geology* **2016**, *44*, 231–234. [[CrossRef](#)]
95. Chen, X.J.; Shu, L.S.; Santosh, M.; Xu, Z.Q. The provenance and tectonic affinity of the Paleozoic meta-sedimentary rocks in the Chinese Tianshan belt: New insights from detrital zircon U-Pb geochronology and Hf-isotope analysis. *J. Asian Earth Sci.* **2014**, *94*, 12–27. [[CrossRef](#)]
96. Bai, J.K.; Chen, J.L.; Tang, Z.; Zhang, Y. The closure time of Junggar Paleozoic oceanic basin: Evidence from Carboniferous de-trital zircon U-Pb geochronology in Kalamaili area. *Geol. Bull. China* **2018**, *37*, 26–38.
97. Li, Y.P.; Li, J.Y.; Sun, G.H.; Zhu, Z.X.; Yang, Z.Q. Basement of Junggar basin; evidence from detrital zircons insandstone of previous Devonian Kalamaili formation. *Acta Petrol. Sin.* **2007**, *23*, 1577–1590.
98. Wu, B.; He, G.Q.; Wu, T.R.; Li, H.J.; Luo, H.L. Discovery of the Buergen ophiolitic melange belt in Xinjiang and its tectonic significance. *Geol. China* **2006**, *33*, 476–486.
99. Dong, S.; Li, Z.; Jiang, L. The Ordovician-Silurian tectonic evolution of the northeastern margin of the Tarim block, NW China: Constraints from detrital zircon geochronological records. *J. Asian Earth Sci.* **2016**, *122*, 1–19. [[CrossRef](#)]
100. Han, Y.G.; Zhao, G.C.; Sun, M.; Eizenhoefer, P.R.; Hou, W.Z.; Zhang, X.R.; Liu, D.X.; Wang, B.; Zhang, G.W. Paleozoic accretionary orogenesis in the Paleo-Asian Ocean: Insights from detrital zircons from Silurian to Carboniferous strata at the northwestern margin of the Tarim Craton. *Tectonics* **2015**, *34*, 334–351. [[CrossRef](#)]
101. Zhao, H.; Liao, Q.A.; Xiao, D.; Luo, T.; Wang, L.Y.; Yin, T.W.; Liu, H.F. Discovery of the Early Silurian alkali basalt and its geological implications in northeastern Junggar, NW China. *Acta Petrol. Sin.* **2018**, *34*, 586–600.
102. Ma, X.H.; Chen, B.; Wang, C.; Yan, X.L. Early Paleozoic subduction of the Paleo-Asian Ocean: Zircon UPb geochronological, geochemical and Sr-Nd isotopic evidence from the Harlik pluton, Xinjiang. *Acta Petrol. Sin.* **2015**, *31*, 89–104.
103. Li, J.T.; He, X.F.; Liu, L.; Yang, P.T.; Liang, B.; Su, H.; Yang, Y.D.; Han, H.M.; Liu, Y.Z.; Dai, Z.H. Ordovician Tectonic Evolution of Harlik in Eastern Tianshan of Xinjiang: Constraints from LA-ICP-MS Zircon U-Pb Geochronology and Geochemistry of Volcanic Rocks. *Geoscience* **2017**, *31*, 460–473.
104. Sun, Y.; Wang, J.B.; Li, Y.C.; Wang, Y.W.; Yu, M.J.; Long, L.L.; Lu, X.Q.; Chen, L. Recognition of Late Ordovician Yudai porphyry Cu (Au, Mo) mineralization in the Kalatag district, Eastern Tianshan terrane, NW China: Constraints from geology, geochronology, and petrology. *Ore Geol. Rev.* **2018**, *100*, 220–236. [[CrossRef](#)]
105. Su, W.B.; Cai, K.D.; Sun, M.; Wan, B.; Wang, X.S.; Bao, Z.H.; Xiao, W.J. Carboniferous volcanic rocks associated with back-arc extension in the western Chinese Tianshan, NW China: Insight from temporal-spatial character, petrogenesis and tectonic significance. *Lithos* **2018**, *310*, 241–254. [[CrossRef](#)]

106. Zha, Y.H.; Wang, G.C.; Shen, T.Y.; Cao, T.L.; Zhang, P. Geochronology and Deformation Stages of Koumenzi Ductile Shear Zone in Harlik Mountain, Xinjiang. *Geotecton. Et Metallog.* **2019**, *44*, 297–310.
107. Wang, Y.F.; Chen, H.Y.; Falloone, J.T.; Han, J.S. The Paleozoic-Mesozoic magmatic evolution of the Eastern Tianshan, NW China: Constraints from geochronology and geochemistry of the Sanchakou intrusive complex. *Gondwana Res.* **2022**, *103*, 1–22. [[CrossRef](#)]
108. Chen, W.; Sun, S.; Zhang, Y.; Xiao, W.J.; Wang, Y.T.; Wang, Q.L.; Jiang, L.F.; Yang, J.T.  $^{40}\text{Ar}/^{39}\text{Ar}$  Geochronology of the Qiugemingtashi-Huangshan Ductile Shear Zone in East Tianshan, Xinjiang, NW China. *Acta Geol. Sin.* **2005**, *79*, 790–804.
109. He, Z.Y.; Wang, B.; Glorie, S.; Su, W.B.; Ni, X.H.; Jepson, G.; Liu, J.H.; Zhong, L.L.; Gillespie, J.; Grave, D.J. Mesozoic building of the Eastern Tianshan and East Junggar (NW China) revealed by low-temperature thermochronology. *Gondwana Res.* **2022**, *103*, 37–53. [[CrossRef](#)]
110. Wang, B.; Shu, L.S.; Faure, M.; Jahn, B.; Cluzel, D.; Charvet, J.; Chung, S.L.; Meffre, S. Paleozoic tectonics of the southern Chinese Tianshan: Insights from structural, chronological and geochemical studies of the Heiyingshan ophiolitic melange (NW China). *Tectonophysics* **2011**, *497*, 85–104. [[CrossRef](#)]
111. Wang, B.R.; Yang, X.S.; Li, S.C.; Teng, C.; Yang, X.J.; Huang, F.Y.; Zhang, X.F.; Cao, J.; Zhou, Y.; Zhang, H.C.; et al. Geochronology, geochemistry, and tectonic implications of early Neoproterozoic granitic rocks from the eastern Beishan Orogenic Belt, southern Central Asian Orogenic Belt. *Precambrian Res.* **2021**, *352*, 106016. [[CrossRef](#)]

**Disclaimer/Publisher's Note:** The statements, opinions and data contained in all publications are solely those of the individual author(s) and contributor(s) and not of MDPI and/or the editor(s). MDPI and/or the editor(s) disclaim responsibility for any injury to people or property resulting from any ideas, methods, instructions or products referred to in the content.